Large differences in the distribution of pelagic biomass as a result of sonar frequency choice

Lloyd Izard, Alejandro Ariza, N. Fonvieille, Éric Goberville, Valentin Djian, Alix Kristiansen, Jean-Benoît Charrassin, Cédric Cotté

Proceedings Of The Royal Society B-biological Sciences
May 2025, Volume 292 Issue 2047 Pages 20242991 (10p.)
https://doi.org/10.1098/rspb.2024.2991
https://archimer.ifremer.fr/doc/00956/106819/

Large differences in the distribution of pelagic biomass as a result of sonar frequency choice

Izard Lloyd [1, *], Ariza Alejandro [2], Fonvieille Nadège [3], Goberville Éric [4], Djian Valentin [4], Kristiansen Alix M. I. [1, 5, 6], Charrassin Jean-Benoît [1], Cotté Cedric [1]

[1] Sorbonne Université, CNRS, IRD, MNHN, Laboratoire d'Océanographie et du Climat: Expérimentations et Approches Numériques (LOCEAN-IPSL), Paris, France
[2] DECOD, Ifremer, INRAE, Institut Agro, Nantes, France
[3] Aix Marseille Univ, Université de Toulon, CNRS, IRD, MIO, Marseille, France
[4] Laboratoire de Biologie des Organismes et des Écosystèmes Aquatiques-BOREA, Sorbonne Université, MNHN, CNRS, IRD, 75005 Paris, France
[5] School of Life and Environmental Sciences, Deakin University, Burwood, Victoria, Australia
[6] EcoBird, Ghent University, Ghent, Belgium

* Corresponding author : Lloyd Izard, email address : lloyd.izard@gmail.com

alejandro.ariza@ifremer.fr ; nadege.FONVIEILLE@univ-amu.fr ; eric.goberville@sorbonne-universite.fr ; valentindjian@gmail.com ; alix.kristiansen@gmail.com ; jean-benoit.charrassin@locean.ipsl.fr ; cedric.cotte@locean.ipsl.fr

Abstract :

Recent efforts to understand the global distribution of pelagic fauna have primarily relied on 38 kHz sonar observations, using water-column backscatter as a proxy of biomass. However, backscatter gradients across ocean provinces are not always consistent with biomass observations from net sampling. This mismatch is particularly evident in temperate to polar transition zones due to changes in the resonance of pelagic fauna, which depends not only on the sonar frequency but also on the size of resonant organs such as fish swimbladders. Here, we investigate how sonar frequency choice changes our vision of pelagic ecosystems across latitudes. We analyse sonar observations at 38 and 18 kHz along with size distributions of swimbladdered fish species across the Indian Ocean Subantarctic Front. Our results show a shift from 38 to 18 kHz dominance towards the poles. More interestingly, backscatter differences across the Subantarctic Front are four times larger at 38 kHz compared to 18 kHz. Size distribution of fish suggests an increase of swimbladder volumes in subantarctic waters, which may explain the observed shift in frequency response. This study highlights the need to address swimbladder resonance variability across latitudes in order to correctly interpret large-scale sonar observations of pelagic fauna.

Keywords : mesopelagic, southern Indian Ocean, swimbladder, micronekton, sound-scattering layers

Introduction

The open-ocean is the Earth's largest habitat (Costello and Chaudhary 2017) and holds most of the animal biomass on the planet (Bar-On et al. 2018). Within this vast space lies the mesopelagic zone, spanning depths from 200 to 1000 m, home to a rich diversity of pelagic fauna, including small fish, crustaceans, squids, and diverse gelatinous life forms (Murray and Hjort 1912). Known as mid-trophic level fauna, these organisms play a key role in marine trophic webs by transferring primary production to higher trophic levels (Choy et al. 2016) and supporting iconic populations of apex predators with patrimonial importance (Iglesias et al. 2023), as well as commercially valuable fish stocks (Christensen and Pauly 1995). By consuming primary production in shallow waters and vertically migrating daily (Brierley et al. 2014), they actively contribute to the export of carbon to the deep ocean and to biogeochemical fluxes on a global scale (Saba et al. 2021).

Quantifying the magnitude of these processes at a regional scale is challenging due to the complexities of deep-sea exploration and the limitations of traditional trawling methods in accurately assessing species distributions beneath the ocean surface (Kaartvedt et al. 2012). Across latitudes and ocean provinces, the problem escalates. Recent efforts to evaluate the global distribution and biomass of pelagic fauna have predominantly relied on ship-borne sonar observations (Irigoien et al. 2014; Proud et al. 2019; Ariza et al. 2022a), as systematic net sampling is unfeasible on such large scales. Sonars are indeed valuable and cost-effective instruments for studying pelagic ecosystems (Benoit-Bird and Lawson 2016). However, translating water-column backscatter into biologically meaningful properties faces limitations when generalised across different oceanic provinces.

One of the greatest challenges is the resonance effect, which occurs when a sonar-detected target not only reflects sound but vibrates at the same frequency, amplifying the signal significantly. In the ocean, this often happens with swimbladdered fish or siphonophores that use gas-filled bladders to regulate buoyancy (Proud et al. 2019). Resonance only occurs when the size of the gas bladder is smaller but close to the wavelength of the emitted frequency (Andreeva 1964). In practice, this means that small organisms in resonance can produce backscatter orders of magnitude stronger than larger organisms out of resonance or that lack gas bladders. Addressing resonance bias and improving biomass estimates require detailed knowledge of gas bladder presence and size—information currently unavailable at the scale of ocean provinces. The problem is further exacerbated by the fact that prominent resonant fish

65 species, such as lanternfish (Myctophidae) and bristlemouths (Gonostomatidae), have
66 functional swimbladders in their early stages, but these often deteriorate or fill with lipids as
67 they mature (Marshall 1960; Kleckner and Gibbs 1978).

68 The occurrence of resonance appears to be widespread in the global ocean, with the
69 exception of polar regions, as suggested by the findings of Chapman et al. (1974). To our
70 knowledge, apart from this pioneering work, there are no multifrequency studies addressing
71 changes in resonance across polar fronts. On the contrary, single-frequency studies at 38 kHz
72 have become the *de facto* standard in ecosystem acoustics in recent years. Indeed, global
73 biogeographies and biomass estimation efforts have predominantly focused on this frequency
74 (Irigoien et al. 2014; Proud et al. 2019; Ariza et al. 2022a; Dornan et al. 2022), hindering the
75 quantification of the consequences of frequency choice when assessing pelagic fauna
76 distribution at large-scale. These acoustic atlases generally reproduce the distribution and
77 density of pelagic fauna across ocean provinces in low- and mid-latitudes compared to net
78 catches (Gjøsæter and Kawaguchi 1980; Backus and Craddock 1977). On the contrary,
79 backscatter and net-based biomass gradients across subpolar fronts are highly inconsistent
80 (Dornan et al. 2019). An illustration of this problem is that 38 kHz backscatter, often regarded
81 as proxy of pelagic biomass, is lower in productive polar systems than in oligotrophic ocean
82 gyres (Ariza et al. 2022a).

83 The Indian sector of the Southern Ocean is not exempt from these constraints in sonar
84 observations. This region presents strong physical and biogeographical gradients along the
85 subtropical convergence (Figure 1; Duhamel et al. 2014). Similarly to the Atlantic and Pacific
86 sectors (Dornan et al. 2019; Escobar-Flores et al. 2018), these transitional waters also exhibit
87 strong declines of 38 kHz backscatter (Béhagle et al. 2016; Boersch-Supan et al. 2017; Izard et
88 al. 2024). The unexpectedly low acoustic signal in this region is surprising, as the presence of
89 islands, associated plateaus, and the dynamic nature of the Antarctic Circumpolar Current
90 contribute to the region's status as one of the most productive areas globally (Lutjeharms and
91 Baker 1980). The subantarctic region surrounding the islands is a recently recognised Area of
92 Ecological Significance for marine top predators, known to feed heavily on mesopelagic prey
93 (Hindell et al. 2020). The relatively low acoustic biomass estimates obtained from studies
94 employing the 38 kHz frequency in the Southern Ocean also seems inconsistent with the known
95 foraging grounds of large populations of apex predators (Cherel et al. 2008; Bestley et al. 2020;
96 Reisinger et al. 2022).

In this study, we explore how alternative sonar frequencies, particularly the less commonly used 18 kHz, reflect the distribution of pelagic fauna compared to the standard 38 kHz frequency across the Southern Ocean subpolar front of the Indian sector. We use acoustic data from three recent consecutive research cruises and employ functional data analysis, clustering, and prediction techniques using environmental drivers to map an alternative 3-dimensional acoustic seascape for the region. Our results are discussed along with fish communities and size distribution charts to explain the change in frequency response towards polar waters. Through these analyses, we assess how 38 and 18 kHz frequencies reflect the distribution of pelagic fauna down to 1000 m depth and discuss their suitability as proxies of pelagic biomass.

Material and methods

Acoustic data acquisition and processing

We used calibrated water-column sonar data collected on board the R/V Marion Dufresne II during the austral summers of 2021, 2022, and 2023 as part of the *THEMISTO* observation program (DOI 10.18142/288), which conducts multidisciplinary oceanographic exploration in subtropical, temperate, subpolar, and polar waters of the Southern Indian Ocean (Figure 1; Table S1). We selected long-range 38 and 18 kHz frequencies to explore the distribution of pelagic fauna down to 1000 m depth, using data from stations surveyed across the three cruises. Our analyses focused on stationary data due to compromised data quality during transit, caused by navigation and inclement weather conditions. Data processing followed standard procedures in MATECHO software (Perrot et al. 2018), including background noise correction (De Robertis and Higginbottom 2007), removal of interferences, attenuated pings and transient noise (Ryan et al. 2015). Data was corrected for sound-speed and absorption using *in situ* temperature and salinity profiles. Acoustic profiles were echointegrated using lower and upper thresholds of -100 and -50 Sv, with a vertical resolution of 10 m and a horizontal resolution of 150 seconds (50 pings), covering depths from 25 to 1000 m. We excluded data during twilight periods from the analysis to avoid diel vertical migration. The resulting profiles were grouped by day and night periods, station, and year, and subsequently averaged into single profiles. These profiles, which included both 38 and 18 kHz frequencies, constitute the unit of analysis, hereinafter referred to as 'observations'. Each observation comprised on average 2 hours of recordings, depending on the duration of operations at station and the percentage of usable data. Our analysis focused on the daytime dataset, consisting of

98 observations spanning from 21° to 56°S latitude and 32° to 83°E longitude (Figure 1). Complementary analyses on the nighttime dataset (82 observations) are also provided in the Supplementary Material.

Figure 1. Study area in the Southern Indian Ocean showing the monthly averaged sea surface (a) temperature (°C), (b) dissolved oxygen (mmol kg^{-1}), and (c) chlorophyll concentration (mg m^{-3}) in January 2021. Acoustic observations were taken from a set of oceanographic stations conducted across three surveys in 2021 (triangles), 2022 (circles), and 2023 (crosses). Dashed lines indicate the position of the Subantarctic Front and the Polar Front (Park et al. 2019). Solid lines demarcate the weighted 75th percentile of overall habitat importance for marine predators, referred to as Areas of Ecological Significance (Hindell et al. 2020).

Statistical analysis

Statistical analyses were performed using R Core Team (2024) version 4.4.2. We investigated the variability in the vertical distribution of pelagic fauna using Functional Data Analysis (R package "fda" version 6.2.0; Ramsay 2024; Figure S1). Discretised profiles at 38 and 18 kHz were converted into spline function systems (Ramsay and Silverman 2005; Ariza et al. 2022b; Izard et al. 2024), and we used the Krzanowski distance method to ascertain the optimal number of spline functions representing acoustic profiles, as in Godard et al. (2020). We chose 25 splines to achieve a vertical resolution of ~40 m (Figure S2), efficient to represent sound scattering layers in the Indian ocean (thickness > 100 m; Béhagle et al. 2016; Boersch-Supan et al. 2017). A higher resolution function system did not significantly increase the fitting performance of acoustic profiles (Figure S3). We applied a Functional Principal Component Analysis to the resulting function coefficients to extract the main modes of variance of acoustic profiles in the dataset, considering both the 38 and 18 kHz frequencies (Figure S4; S5). We applied the broken stick method (R package "PCDimension" version 1.1.13; Coombes and Wang 2022) to determine the most important modes of variance to be retained in subsequent analyses, and selected the first four principal components, which together explained 71% (32+15+13+8%) of the total profile variance in the dataset. Sampling locations were clustered using these four principal components to summarise the main modes of profile variance at 38 and 18 kHz, using agglomerative hierarchical clustering with the Ward linkage method (R package "stats"; R version 4.4.2). We computed the median and interquartile range of acoustic profiles by clusters and frequency to visualise the main vertical distribution patterns of sound-scattering fauna at each ocean system.

To understand the influence of oceanographic conditions on these patterns, we expanded our observations to cover the area between 21° to 56°S latitude and 32° to 83°E longitude, with

a resolution of 1/4 degree (Figure S7). We projected the distribution of acoustic backscatter in the area using three environmental predictors known to shape the distribution of pelagic fauna at large scales (Bianchi et al. 2013; Proud et al. 2019; Ariza et al. 2022a): temperature (°C), dissolved oxygen (mmol kg^{-1}), and satellite-derived chlorophyll concentration (mg m^{-3}) (Figure S8). Environmental data were sourced from the E.U. Copernicus Marine Service Information. Temperature profiles were obtained from the Global Ocean Physics Reanalysis (1/12°; 10.48670/moi-00021), while dissolved oxygen and chlorophyll profiles were retrieved from the Global Ocean Biogeochemistry Analysis and Forecast (1/4°; 10.48670/moi-00015). Similar to the acoustic data analysis, we defined one environmental observation as the simultaneous profiles of these three variables (Figure S9). We smoothed the data and performed a Functional Principal Component Analysis on the monthly profiles for January, February, and March of 2021, 2022, and 2023. We retained two principal components (capturing ~90% of the variance, as supported by the broken-stick method; Figure S10). The initial variability of the system was reduced to eigenfunctions and their associated principal component maps (Figure S11, S12). We conducted optimised Random Forest models (R package "h2o" version 3.46.0.6; Fryda et al. 2024) to predict acoustic principal component values from the environmental principal components for each period (Jan., Feb. March 2021, 2022 and 2023). Predictive performance tests and details about modelling are found in the Supplementary Material (Table S2; Figure S13 to S15). The resulting set of maps represented unique predicted modes of variability for each period (Figure S16). Using the principal component maps in conjunction with vertical modes, we reconstructed observations (38 and 18 kHz profiles) for each period grid point and computed their respective integrated acoustic energy (NASC, m^2 nmi^{-2}) from 25 to 1000 m depth. Finally, we calculated the mean and standard deviation of all NASC predictions across all periods to represent the distribution of acoustic backscatter in the area (Figure S20).

Target strength modelling

To understand the observed variations in frequency response, we used simple scattering models to simulate the acoustic response of lanternfish (Myctophidae), hatchetfish (Sternoptychidae), and species of the genus *Cyclothone* (Gonostomatidae). These were the dominant swimbladdered fish responsible for sound-scattering on both sides of the Subantarctic Front, based on net sampling abundance data (see section below) and previous studies (Duhamel et al. 2014; Iwami and Kubodera, 1990; Figure S25). We considered two scenarios: one where most of the backscatter is caused by resonance of gas-filled swimbladdered fish, and another where most of the backscatter is caused by fish without a functional swimbladder. We

modelled the resonance scenario using Andreeva (1964)'s model adapted for prolate gas spheroids by Weston (1967) and parameterised for mesopelagic fish tissue and swimbladder properties as in Ariza et al. (2016). Resonance was represented relative to fish standard length based on body-swimbladder size relationships available for lanternfish and hatchetfish in Saenger (1989), and for *Cyclothone* species in Sarmiento-Lezcano et al. (2023). In the non-resonant scenario, we used the Distorted Wave Born Approximation (DWBA) model (R package "ZooScatR" version 0.61; Gastauer et al. 2019), with fish body parametrisation as described by Proud et al. (2019). We conducted both modelling exercises for fish lengths ranging from 10 to 80 mm, assuming a vertical distribution between 100 to 900 m (Supplementary material, Figure S23).

Fish species and size distributions

Our acoustic observations and models were further validated using size distribution data of lanternfish, hatchetfish and *Cyclothone* spp. To achieve this, we used horizontal tows targeting the core of the main DSL at 38 kHz during the 2022 campaign, north and south of the Subantarctic Front (Figure S24). The net used was a Mesopelagos trawl (Meillat 2012), a non-closing device of 65 m^2 mouth area and 44 m length. The trawl had a mesh size of 30 mm in the wings, reducing to 4 mm in the codend (sampling details in Table S3). Size distributions on either side of the front were compared against resonance sizes predicted by the model. Additionally, we included historical data from oblique IKMT tows, recovered from the Scripps Marine Vertebrate Collection and from Iwami and Kubodera (1990). Our results from net-sampling, conducted simultaneously with acoustic recordings, were compared with this historical data. This comparison aimed to determine whether the changes in swimbladdered fish species across the Subantarctic Front are consistent with previous studies and whether they explain the signal variations detected by sonar (Figure S25).

Results and discussion

Acoustic seascape regionalisation

The classification of acoustic profiles yielded four spatially coherent clusters, termed "echobiomes" following Ariza et al. (2022). These echobiomes were distributed across four distinct ocean regions (Figure 2a-b). From north to south, they encompassed subtropical, temperate, subpolar, and polar waters. The distribution was similar using the nighttime dataset (Figure S6). The shape of acoustic profiles within each echobiome reflects the vertical

distribution and density of sound-scattering fauna, exhibiting prominent peaks indicative of the main sound scattering layers within the water column. While the vertical distribution of sound scattering layers at 38 and 18 kHz profiles remain relatively consistent within each echobiome, variations emerge when comparing profiles across latitudes. Subtropical (Figure 2c-g) and temperate (Figure 2d-h) echobiomes exhibit two distinct sound scattering layers distributed at depths of 0-200 m and 400-700 m, separated by zones with markedly reduced signal.

This acoustic seascape configuration aligns with previous observations in mid-latitude regions worldwide (Ariza et al. 2022a). The deeper distribution of sound scattering layers in subtropical compared to temperate waters likely results from increased light penetration that drives pelagic fauna to deeper waters (Aksnes et al. 2017). Conversely, the vertically integrated backscatter of temperate acoustic profiles exceeds that of subtropical profiles from two- to three-fold (see NASC in Figure 2), similarly to biomass differences observed through net-sampling in similar ocean systems (Gjøsæter and Kawaguchi 1980). Subpolar (Figure 2e-i) and polar (Figure 2f-j) echobiomes display less stratified profiles, characterised by less-prominent layers spanning from 400 to 1000 m depth. While the epipelagic layer remains well-developed in subpolar waters, similar to subtropical and temperate echobiomes, it experiences a notable reduction further south in polar waters. In this case, water-column backscatter decreases south of the subpolar front, a trend that appears inconsistent with the relative biomass differences observed through net-sampling (Gjøsæter and Kawaguchi, 1980). Despite these inconsistencies between sonar and net-sampling, our observations at 38 kHz align well with previous acoustic studies in the Indian Ocean (Béhagle et al. 2016; Boersch-Supan et al. 2017; Izard et al. 2024; Kang et al. 2024) and with global acoustic biogeographies (Proud et al. 2018; Ariza et al. 2022a) based on the same frequency.

Figure 2. Acoustic seascape classification based on the shape of 38 and 18 kHz daytime profiles, which represents the vertical distribution of sound-scattering fauna. (a) Agglomerative hierarchical clustering shows (b) four classes distributed across latitudinal bands in the Southern Indian Ocean. The black lines on the map represent the Subantarctic Front and the Polar Front (Park et al. 2019). Acoustic seascape classes correspond to subtropical (red), temperate (yellow), subpolar (violet) and polar (black) regions. Distinct vertical distributions of sound-scattering fauna are observed across regions at both (c-f) 38 kHz and (g-j) 18 kHz frequencies. In these profiles, the median (solid line) and interquartile ranges (shaded) are depicted. The vertical integration of median and interquartile values is provided at the base of profiles as a proxy of total water column biomass (NASC: Nautical Area Scattering Coefficient, m^2 nmi^{-2}). (k-n) The difference between the 38 and 18 kHz profiles highlights the depths where one frequency dominates the other within each region: positive (negative) values correspond to 18 kHz (38 kHz) dominance.

Different frequency response of pelagic fauna across regions

Despite the vertical distribution of sound scattering layers being fairly close at 38 and 18 kHz, the subtraction of both profiles reveals important differences in the backscatter magnitude of these layers. The vertical structure of these differences also changes from north to south across echobiomes. Major frequency anomalies occur at subtropical and temperate latitudes, where 38 kHz consistently exhibits higher backscatter in both shallow and deep scattering layers (Figure 2k-l). This pattern reverses in subpolar and polar echobiomes, where 18 kHz became dominant, although the anomalies are less pronounced, particularly in deep mesopelagic layers (Figure 2m-n). These anomalies impact the total backscatter contained in the water column across the Southern Indian Ocean, a common proxy for global animal biomass (Irigoien et al. 2014; Proud et al. 2017; Ariza et al. 2022a).

Our statistical model allowed us to scale up these observations regionally by reconstructing acoustic profiles and subsequently estimating integrated water-column backscatter across the region. Uncertainty metrics indicate strong agreement between predicted and observed backscatter profiles (see model performance metrics in supplementary methods, Table S2; Figure S17 and S18). In addition to uncertainty analyses, the range and geographical distribution of water-column backscatter is also consistent with those reported by Ariza et al. (2022). At 38 kHz (Figure 3a), water column backscatter decreases from north to south, peaking between 30 and 40°S (~2500 m^2 nmi^{-2}) and reaching minimum values between 40 and 55°S (~500 m^2 nmi^{-2}), aligning with recently identified high- and low-density micronekton areas in the region (Wan & Chen 2024). At 18 kHz (Figure 3b), we observe a moderate maximum between 35 and ~55°S (~1500 m^2 nmi^{-2}), with significant lower backscatter north and south of this region (~500 m^2 nmi^{-2}). If water-column backscatter serves as a reliable proxy for pelagic biomass, our results reveal important inconsistencies in the latitudinal distribution of biomass between 38 and 18 kHz frequencies. Although this pattern varied slightly depending on the month and year (Figure S19), the north-to-south shift in dominant frequency from 38 to 18 kHz (Figure 3c; S21) consistently aligned with the Subantarctic Front (Park et al. 2019) and earlier observations of frequency response changes near subpolar fronts (Chapman et al. 1974).

Figure 3. Modelled daytime water-column backscatter (nautical area scattering coefficient; NASC, m^2 nmi^{-2}), a variable often used as a proxy for pelagic fauna density. Backscatter is integrated from 25 to 1000 m depth and measured at (a) 38 kHz, (b) 18 kHz, and (c) 18 minus 38 kHz. Dotted lines on the map represent the Subantarctic Front and the Polar Front (Park et al. 2019). Solid lines delineate the 75th percentile for Areas of Ecological

Significance identified using marine predator trajectories (Hindell et al. 2020). In panel (c), note how pelagic fauna changes the frequency response across latitude. North (South) of the Subpolar Front is dominated by 38 kHz (18 kHz).

Why does frequency response change across the Subantarctic Front?

There is ample evidence of a strong biogeographical transition across the Southern Ocean subpolar fronts (Duhamel et al. 2014; Sutton et al. 2017). Given its alignment with the transition zone observed in this study, the question arises as to how these faunal changes could reproduce this specific vertical and latitudinal frequency response pattern at 38 and 18 kHz. Lanternfish (Myctophidae), hatchetfish (Sternoptychidae), lightfish (Photichthyidae), and species of the genus Cyclothone (Gonostomatidae) are the most prevalent swimbladdered fish in mesopelagic waters (Marshall 1960). While all these fishes can potentially resonate when insonified at both 38 and 18 kHz, hatchetfish and lightfish virtually disappear south of the Subantarctic Front (Iwami and Kubodera 1990; Figure S25). This, *per se*, may explain the drop in backscatter at both frequencies in subpolar waters (Figure 3a-b), but it does not explain the latitudinal shift in resonance frequency (Figure 3c). Scattering models predict that if gas-filled swimbladdered fish were entirely absent from subpolar waters, 38 kHz should consistently dominate over 18 kHz, irrespective of fish size (Figure 4a). The only scenario in which mesopelagic sound scattering layers would exhibit a stronger signal at 18 kHz is if polar waters were dominated by fish with larger resonant swimbladders (Figure 4a).

Following this rationale, we simulated the acoustic response of the three swimbladdered fish families found during net sampling that could potentially induce a resonance shift across the Subantarctic Front (Figure 4a). Namely, lanternfish (Myctophidae), hatchetfish (Sternoptychidae), and bristlemouths (Gonostomatidae). For Gonostomatidae, we restricted our simulation to species within the genus *Cyclothone* due to their widespread possession of swimbladders, unlike other species of the family (Marshall 1960). Additionally, *Cyclothone* species have been previously linked to resonance at 38 kHz (Ariza et al. 2016; Peña et al. 2014, 2023). Our simulations show that at 500 m depth, 18 kHz resonance becomes dominant over 38 kHz when swimbladders exceed a radius of ~1 mm, corresponding to standard fish lengths of ~35-40 mm for lanternfish, hatchetfish, and *Cyclothone* species (Figure 4a). We focused on resonance at 500 m, as this depth showed the greatest difference between 38 kHz and 18 kHz (Figure 2k-n). However, across depths ranging from 100 to 900 m, the transition in resonance frequency could theoretically occur in fish sizes between 20 and 45 mm (Figure S23). In our

simulations, 18 kHz resonance was attributed exclusively to lanternfish, as they are the only swimbladdered fish family still present in the southern region, where 18 kHz dominates. In contrast, hatchetfish and small Cyclothone species with functional gas-filled swimbladders are rare beyond the subpolar front (Figure S25; Iwami and Kubodera 1990; Duhamel et al. 2014). Even if small *Cyclothone* species were present in polar waters, their gas-bladders never surpass an equivalent spherical radius of 1 mm (Marshall 1960; Kleckner and Gibbs 1978), making them unlikely to resonate at 18 kHz (Figure 4a, b).

This theoretical size distribution, derived from resonance modelling, aligns well with our net-sampling observations. Trawls targeting the main mesopelagic sound scattering layer revealed that fish north of the Subantarctic Front are predominated by fish smaller than 40 mm in length, whereas south of the front, dominant fish sizes range from 35 to 70 mm (Figure 4b). This size shift corresponds well with the predicted resonance switch of our model (Figure 4a). North of the front, swimbladdered species comprised small hatchetfish, lanternfish, and Cyclothone. South of the front, catches were composed primarily of larger lanternfish, with Cyclothone occurring only sporadically and hatchetfish entirely absent. These findings are also consistent with historical fishing data from museum collections and literature (Figure S25; Iwami and Kubodera 1990). Notably, of the seven *Cyclothone* species reported in the Indian Ocean, only the largest species *C. microdon* appears to reach polar waters, based on our literature review (Figure S25). Furthermore, historical data suggest that larger-bodied lanternfish persist south of the Subantarctic Front (Figure S25) and, unlike *Cyclothone* species, they can still present gas-filled swimbladders beyond 40 mm in length (Kleckner and Gibbs 1972).

In summary, both our observations and literature review suggest an increase in swimbladder size toward polar waters, which aligns with the observed resonance shift from 38 to 18 kHz. In principle, this finding may seem contradictory to recent observations in the Atlantic sector of the Southern Ocean, where swimbladders were reported to decrease toward high latitudes (Dornan et al. 2019). However, we believe that both scenarios are plausible, depending on frequency, swimbladder size, and latitude. Dornan et al. (2019) used a 38 kHz echosounder between ~ 52°S and 60°S, extending to the southern boundary of the Antarctic circumpolar current. In contrast, our study, which incorporate both 38 and 18 kHz, spans a broader latitudinal range, from ~20°S to ~55°S, but does not extend as far south, where there may indeed be a total absence of gas-filled swimbladders. That said, Dornan et al. (2019) still reported the presence of gas-bearing fish near the subpolar front, consistent with our findings.

Unfortunately, resonance at 18 kHz could not be reported in Dornan et al. (2019) as the authors lacked this frequency at the time of surveying. Hence, considering both studies, we believe that an intermediate region likely exists between temperate and polar waters where large gas-bearing fish dominate over smaller fish, before swimbladders disappear further south. This may indeed explain the shift of resonance from 38 to 18 kHz.

Finally, the contribution of other gas-bearing organisms such as siphonophores to latitudinal changes in frequency response cannot be ruled out (Proud et al. 2019). Unfortunately, limited knowledge on siphonophore distribution, vertical positioning, and gas bladder morphology at large scale constraints further investigation. A recent study, though, indicates that calycophoran siphonophores —lacking gas bladders—dominate at 200–500 m around the tropical and subtropical regions (Claver et al. 2024). The same study shows that physonectid siphonophores with gas bladders become more prevalent below 500 m and dominate bathypelagic depths. These findings imply that, at least at low- and mid-latitudes, mesopelagic sound scattering is unlikely to be primarily driven by siphonophores. However, further observations at higher latitudes and with greater vertical resolution are required to fully understand their role in ocean resonance.

Figure 4. (a) Modelled target strength of Cyclothone species, hatchetfish (Sternoptychidae) and lanternfish (Myctophidae) across body lengths of 10-80 mm, assuming a vertical distribution at 500 m depth. Target strength simulations are based on the occurrence of swimbladdered fish species at each side of the Subantarctic Front: Cyclothone, Sternoptychidae and Myctophidae in the north, dominated by 38 kHz; Myctophidae in the south, dominated by 18 kHz. (b) Size distribution of the same fish families normalised by sampling effort (individuals per hour) for regions north and south of the Subantarctic Front. (c) Observed daytime water-column backscatter at 38 and 18 kHz, expressed as the nautical area scattering coefficient (NASC, m^2 nmi^{-2}), integrated over depths of 25 to 1000 m. NASC values are shown for regions spanning latitudes from 30°S to 55°S, north and south of the Subantarctic Front.

Challenges and opportunities of resonance changes across ocean provinces

Allocating resonance to specific organisms across ocean provinces remains challenging, yet both scattering models and observations highlight the critical consequences of neglecting this effect: biomass estimations can be biased by orders of magnitude (Godø et al. 2009). To illustrate this problem, we compared integrated water-column backscatter at 38 and 18 kHz north and south of the Subantarctic Front, where frequency dominance shifts (Figure 4c). We observe approximately four times more water-column backscatter north of the Subantarctic Front at 38 kHz, whereas the difference is marginal at 18 kHz (1.1 times). This suggests that relying solely on 38 kHz as a proxy for pelagic biomass distribution could overestimate biomass

at mid-latitudes by a factor of four with respect to high-latitudes, solely due to resonance effects rather than actual changes in biomass distribution. At night, this discrepancy becomes even greater: 4.9 times higher at 38 kHz and 1.6 times at 18 kHz (Figure S22). These differences between day and night illustrate how resonance varies with the vertical migration of organisms (Figure S23), introducing further uncertainty when comparing sonar data across oceanic provinces. Unfortunately, this issue is often overlooked when using a single frequency for biomass estimation.

On the bright side, multifrequency acoustic surveys offer a unique advantage: backscatter anomalies can help delineate faunal transitions across oceanic provinces. A good illustration is the strong match between the 18-38 kHz transition zone identified in this study and the northern boundary of an Area of Ecological Significance for subantarctic marine top predators (Hindell et al. 2020). Our observations at 18 kHz reconcile backscatter levels with the foraging grounds of the world's largest populations of marine mammals and seabirds, where mesopelagic fish represents an important component of their diet. This trophic relationship has been reported for king penguins (Raclot et al. 1998, Cherel et al. 2010), fur seals (Cherel et al. 2007), elephant seals (Cherel et al. 2008), albatrosses and petrels (Connan et al. 2007).

Conclusion

In this study, we characterise the acoustic seascape of the Southern Indian Ocean at 38 and 18 kHz, revealing changes in frequency response and resonance of pelagic fauna across the Subantarctic Front. These changes pose major challenges in accurately estimating biomass across latitudes but simultaneously provide a cost-effective tool to track and monitor biogeographic boundaries (Kloser et al. 2009). Inspired by Chapman et al.'s (1974) concept of "*dividing the world's oceans into reverberation provinces*", we advocate for considering resonance into acoustic biomass estimates and emphasise the importance of accounting for this effect at the scale of ocean provinces. Achieving this requires an internationally coordinated effort to elaborate a "Global Ocean Swimbladder Atlas", detailing size, vertical, and horizontal distribution of swimbladders across provinces (Dornan et al. 2019; Sarmiento-Lezcano et al. 2023; Peña et al. 2023). While this is a formidable challenge, acoustic echosounders still remain our best approach for observing pelagic ecosystem processes at the spatio-temporal scales on which they occur (Godø et al. 2014). With the looming threats of climate change (Sallée et al. 2018) and marine heatwaves (Azarian et al. 2023) in the Southern Indian Ocean, ship-borne acoustic observations can play an important role in monitoring and anticipating such impacts.

Acknowledgements

The authors thank the captains and crews of the R/V Marion Dufresne II and the Genavir crew. They also express their sincere gratitude to Clara Péron (MNHN) for identifying the fish species from the 2022 THEMISTO cruise. Through LI Ph.D., this work was funded by the French Ministry for Education and Research (ED 129). The THEMISTO cruises were supported by the Flotte Océanographique Française, the CNES OSTST Tosca KERTREND-SAT, the CNRS Antarctic Workshop Zone and the TAAF National Nature Reserve programs. The OISO program is supported by the French institutes INSU (Institut National des Sciences de l'Univers), IPSL (Institut Pierre Simon Laplace), IPEV (Institut Polaire Paul Emile Victor) and Sorbonne University (OSU Ecce Terra). The SWINGS project was supported by the Flotte Océanographique Française (10.17600/18001925), Agence Nationale de la Recherche (ANR 19-CE01-0012), CNRS/ INSU (Centre National de la Recherche Scientifique/Institut National des Sciences de l'Univers) through its LEFE actions, Université de Bretagne Occidentale, and IsBlue project, Interdisciplinary graduate school for the blue planet (ANR 17-EURE-0015) and co-funded by a grant from the French government under the program 'Investissements d'Avenir" embedded in France 2030.

References

Andreeva, I. B. (1974). Scattering of sound by air bladders of fish in deep sound-scattering ocean layers. Sov. Phys. Acoust., 10, 17-20.

Aksnes, D.L., Røstad, A., Kaartvedt, S., Martinez, U., Duarte, C.M. and Irigoien, X., 2017. Light penetration structures the deep acoustic scattering layers in the global ocean. Science Advances, 3(5), p.e1602468.

Ariza, A., Landeira, J.M., Escánez, A., Wienerroither, R., de Soto, N.A., Røstad, A., Kaartvedt, S. and Hernández-León, S., 2016. Vertical distribution, composition and migratory patterns of acoustic scattering layers in the Canary Islands. Journal of Marine Systems, 157, pp.82-91.

Ariza, A., Lengaigne, M., Menkes, C., Lebourges-Dhaussy, A., Receveur, A., Gorgues, T., Habasque, J., Gutiérrez, M., Maury, O. and Bertrand, A., 2022a. Global decline of pelagic fauna in a warmer ocean. Nature Climate Change, 12(10), pp.928-934.

Ariza, A., Lebourges-Dhaussy, A., Nerini, D., Pauthenet, E., Roudaut, G., Assunção, R., Tosetto, E., & Bertrand, A., 2022b. Acoustic seascape partitioning through functional data analysis. Journal of Biogeography, 00, 1–15. https://doi.org/10.1111/jbi.14534

Azarian, C., Bopp, L., Pietri, A., Sallée, J.B. and d'Ovidio, F., 2023. Current and projected patterns of warming and marine heatwaves in the Southern Indian Ocean. Progress in Oceanography, 215, p.103036.

Backus, R.H. and Craddock, J.E., 1977. Atlantic mesopelagic zoogeography. collections, 274, p.331.

Bar-On, Y.M., Phillips, R. and Milo, R., 2018. The biomass distribution on Earth. Proceedings of the National Academy of Sciences, 115(25), pp.6506-6511.

Béhagle, N., Cotté, C., Ryan, T.E., Gauthier, O., Roudaut, G., Brehmer, P., Josse, E. and Cherel, Y., 2016. Acoustic micronektonic distribution is structured by macroscale oceanographic processes across 20–50 S latitudes in the South-Western Indian Ocean. Deep Sea Research Part I: Oceanographic Research Papers, 110, pp.20-32.

Benoit-Bird, K.J. and Lawson, G.L., 2016. Ecological insights from pelagic habitats acquired using active acoustic techniques. Annual review of marine science, 8, pp.463-490.

Bianchi, D., Galbraith, E.D., Carozza, D.A., Mislan, K.A.S. and Stock, C.A., 2013. Intensification of open-ocean oxygen depletion by vertically migrating animals. Nature Geoscience, 6(7), pp.545-548.

Boersch-Supan, P.H., Rogers, A.D. and Brierley, A.S., 2017. The distribution of pelagic sound scattering layers across the southwest Indian Ocean. Deep Sea Research Part II: Topical Studies in Oceanography, 136, pp.108-121.

Bestley, S., Ropert-Coudert, Y., Bengtson Nash, S., Brooks, C.M., Cotté, C., Dewar, M., Friedlaender, A.S., Jackson, J.A., Labrousse, S., Lowther, A.D. and McMahon, C.R., 2020. Marine ecosystem assessment for the

Southern Ocean: birds and marine mammals in a changing climate. Frontiers in Ecology and Evolution, 8, p.566936.

Brierley, A.S., 2014. Diel vertical migration. Current biology, 24(22), pp.R1074-R1076.

Cherel, Y., Hobson, K.A., Guinet, C. and Vanpe, C., 2007. Stable isotopes document seasonal changes in trophic niches and winter foraging individual specialization in diving predators from the Southern Ocean. Journal of Animal Ecology, 76(4), pp.826-836.

Cherel, Y., Ducatez, S., Fontaine, C., Richard, P. and Guinet, C., 2008. Stable isotopes reveal the trophic position and mesopelagic fish diet of female southern elephant seals breeding on the Kerguelen Islands. Marine Ecology Progress Series, 370, pp.239-247.

Cherel, Y., Fontaine, C., Richard, P. and Labatc, J.P., 2010. Isotopic niches and trophic levels of myctophid fishes and their predators in the Southern Ocean. Limnology and oceanography, 55(1), pp.324-332.

Christensen, V. and Pauly, D., 1995. Fish production, catches and the carrying capacity of the world oceans.

Connan, M., Cherel, Y. and Mayzaud, P., 2007. Lipids from stomach oil of procellariiform seabirds document the importance of myctophid fish in the Southern Ocean. Limnology and Oceanography, 52(6), pp.2445-2455.

Coombes KR, Wang M (2022). PCDimension: Finding the Number of Significant Principal Components. R package version 1.1.13, https://CRAN.R-project.org/package=PCDimension.

Costello, M.J. and Chaudhary, C., 2017. Marine biodiversity, biogeography, deep-sea gradients, and conservation. Current Biology, 27(11), pp.R511-R527.

Chapman, R.P., Bluy, O.Z., Adlington, R.H. and Robison, A.E., 1974. Deep scattering layer spectra in the Atlantic and Pacific Oceans and adjacent seas. The Journal of the Acoustical Society of America, 56(6), pp.1722-1734.

Choy, C., Wabnitz, C., Weijerman, M., Woodworth-Jefcoats, P., Polovina, J., 2016. Finding the Way to the Top: How the Composition of Oceanic Mid-Trophic Micronekton Groups Determines Apex Predator Biomass in the Central North Pacific. Marine Ecology Progress Series 549, 9–25. https://doi.org/10.3354/meps11680

Claver, C., Rodríguez-Ezpeleta, N., Irigoien, X. and Canals, O., 2024. Global distribution patterns of siphonophores across horizontal and vertical oceanic gradients. Open Research Europe, 4, p.177.

De Robertis, A. and Higginbottom, I., 2007. A post-processing technique to estimate the signal-to-noise ratio and remove echosounder background noise. *ICES Journal of Marine Science*, *64*(6), pp.1282-1291.

Duhamel, G., Hulley, P.-A., Causse, R., Koubbi, P., Vacchi, M., Pruvost, P., et al. (2014). "Chapter 7. Biogeographic patterns of fish," in Biogeographic Atlas of the Southern Ocean, eds C. De Broyer, P. Koubbi, H. Griffiths, B. Raymond, C. d'Udekem d'Acoz, A. Van de Putte, et al. (Cambridge: Scientific Committee on Antarctic Research), 327–362.

Dornan, T., Fielding, S., Saunders, R.A. and Genner, M.J., 2019. Swimbladder morphology masks Southern Ocean mesopelagic fish biomass. Proceedings of the Royal Society B, 286(1903), p.20190353.

Dornan, T., Fielding, S., Saunders, R.A. and Genner, M.J., 2022. Large mesopelagic fish biomass in the Southern Ocean resolved by acoustic properties. Proceedings of the Royal Society B, 289(1967), p.20211781.

Escobar-Flores, P.C., Driscoll, R.L. and Montgomery, J.C., 2018. Spatial and temporal distribution patterns of acoustic backscatter in the New Zealand sector of the Southern Ocean. Marine Ecology Progress Series, 592, pp.19-35.

Fryda T, LeDell E, Gill N, Aiello S, Fu A, Candel A, Click C, Kraljevic T, Nykodym T, Aboyoun P, Kurka M, Malohlava M, Poirier S, Wong W (2024). h2o: R Interface for the 'H2O' Scalable Machine Learning Platform. R package version 3.46.0.6, https://github.com/h2oai/h2o-3.

Gastauer, S., Chu, D. & Cox, M. J. ZooScatR - An R package for modelling the scattering properties of weak scattering targets using the distorted wave Born approximation. The Journal of the Acoustical Society of America 145, EL102–EL108 (2019).

Gjøsæter, J. and Kawaguchi, K., 1980. A review of the world resources of mesopelagic fish.

Global Ocean Biogeochemistry Analysis and Forecast. E.U. Copernicus Marine Service Information (CMEMS). Marine Data Store (MDS). DOI: 10.48670/moi-00015) (Accessed on 09 Dec. 2024).

Global Ocean Physics Reanalysis. E.U. Copernicus Marine Service Information (CMEMS). Marine Data Store (MDS). DOI: 10.48670/moi-00021) (Accessed on 09 Dec. 2024).

Godard, M., Manté, C., Guinet, C., Picard, B. and Nerini, D., 2020. Diving behavior of mirounga leonina: a functional data analysis approach. Frontiers in Marine Science, 7, p.595.

Godø, O.R., Patel, R. and Pedersen, G., 2009. Diel migration and swimbladder resonance of small fish: some implications for analyses of multifrequency echo data. ICES Journal of Marine Science, 66(6), pp.1143-1148.

Godø, O.R., Handegard, N.O., Browman, H.I., Macaulay, G.J., Kaartvedt, S., Giske, J., Ona, E., Huse, G. and Johnsen, E., 2014. Marine ecosystem acoustics (MEA): quantifying processes in the sea at the spatio-temporal scales on which they occur. ICES Journal of Marine Science, 71(8), pp.2357-2369.

Hindell, M.A., Reisinger, R.R., Ropert-Coudert, Y., Hückstädt, L.A., Trathan, P.N., Bornemann, H., Charrassin, J.B., Chown, S.L., Costa, D.P., Danis, B. and Lea, M.A., 2020. Tracking of marine predators to protect Southern Ocean ecosystems. Nature, 580(7801), pp.87-92.

Iglesias, I.S., Santora, J.A., Fiechter, J. and Field, J.C., 2023. Mesopelagic fish are important prey for a diversity of predators.

Irigoien, X., Klevjer, T.A., Røstad, A., Martinez, U., Boyra, G., Acuña, J.L., Bode, A., Echevarria, F., Gonzalez-Gordillo, J.I., Hernandez-Leon, S. and Agusti, S., 2014. Large mesopelagic fish biomass and trophic efficiency in the open ocean. Nature communications, 5(1), p.3271.

Iwami, T., and Kubodera, T. (1990). Mesopelagic fish collected with 10-foot IKPT in the Indian sector of the Antarctic Ocean and its neighboring waters during the JARE-28 cruise, 1987 (Eleventh Symposium on Polar Biology). In Proceedings of the NIPR Symposium on Polar Biology (Vol. 3, pp. 64-70). National Institute of Polar Research.

Izard, L., Fonvieille, N., Merland, C., Koubbi, P., Nerini, D., Habasque, J., Lebourges-Dhaussy, A., Monaco, C.L., Roudaut, G., d'Ovidio, F. and Charrassin, J.B., 2024. Decomposing acoustic signal reveals the pelagic response to a frontal system. Journal of Marine Systems, 243, p.103951.

Kaartvedt, S., Staby, A. and Aksnes, D.L., 2012. Efficient trawl avoidance by mesopelagic fish causes large underestimation of their biomass. Marine Ecology Progress Series, 456, pp.1-6.

Kang, M., Simanungkalit, F., Kang, D., Jung, J., Kim, J., Song, S., Kim, Y., Kang, D.J. and Nam, S., 2024. Latitudinal influences on sound scattering layer characteristics in the Southwestern Indian Ocean: insights into oceanographic environmental interactions. *Frontiers in Marine Science*, *11*, p.1481531.

Kleckner, R., Gibbs, R., 1972. Swimbladder Structure of Mediterranean Midwater Fishes and a Method of Comparing Swimbladder Data with Acoustic Profiles, in: Mediterranean Biological Studies Final Report. Smithsonian Institution.

Klevjer, T.A., Irigoien, X., Røstad, A., Fraile-Nuez, E., Benítez-Barrios, V.M. and Kaartvedt, S., 2016. Large scale patterns in vertical distribution and behaviour of mesopelagic scattering layers. Scientific Reports, 6(1), p.19873.

Kloser, R.J., Ryan, T.E., Young, J.W. and Lewis, M.E., 2009. Acoustic observations of micronekton fish on the scale of an ocean basin: potential and challenges. ICES Journal of Marine Science, 66(6), pp.998-1006.

Lutjeharms, J.R.E. and Baker Jr, D.J., 1980. A statistical analysis of the meso-scale dynamics of the Southern Ocean. Deep Sea Research Part A. Oceanographic Research Papers, 27(2), pp.145-159.

Marshall, N., 1960. Swimbladder structure of deep-sea fishes in relation to their systematics and biology, Discovery Reports, Vol. XXXI.

Meillat, M., 2012. Essais du chalut mésopélagos pour le programme MYCTO 3D - MAP de l"IRD, à bord du Marion Dufresne (du 10 au 21 août 2012). Rapport de mission, Ifremer.

Murray, J., Hjort, J., Gran, H.H. and Helland-Hansen, B., 1912. The depths of the ocean: a general account of the modern science of oceanography based largely on the scientific researches of the Norwegian steamer Michael Sars in the North Atlantic (Vol. 37). Macmillan.

Peña, M., Olivar, M.P., Balbín, R., Lopez-Jurado, J.L., Iglesias, M. and Miquel, J., 2014. Acoustic detection of mesopelagic fish in scattering layers of the Balearic Sea (western Mediterranean). Canadian Journal of Fisheries and Aquatic Sciences, 71(8), pp.1186-1197.

Peña, M., Andrès, L. and González-Quirós, R., 2023. Target strength of Cyclothone species with fat-filled swimbladers. Journal of Marine Systems, 240, p.103884.

Park, Y.-H., Park, T., Kim, T.-W., Lee, S.-H., Hong, C.-S., Lee, J.-H., Rio, M.-H., Pujol, M.I., Ballarotta, M., Durand, I., Provost, C., 2019. Observations of the Antarctic Circumpolar Current over the Udintsev Fracture Zone, the narrowest choke point in the Southern Ocean. J. Geophys. Res. Oceans 124, 4511–4528. https://doi.org/10.1029/2019JC015024.

Perrot, Y., Brehmer, P., Habasque, J., Roudaut, G., Behagle, N., Sarré, A. and Lebourges-Dhaussy, A., 2018. Matecho: an open-source tool for processing fisheries acoustics data. Acoustics Australia, 46, pp.241-248.

Proud, R., Cox, M.J. and Brierley, A.S., 2017. Biogeography of the global ocean's mesopelagic zone. *Current Biology*, *27*(1), pp.113-119.

Proud, R., Cox, M.J., Le Guen, C. and Brierley, A.S., 2018. Fine-scale depth structure of pelagic communities throughout the global ocean based on acoustic sound scattering layers. Marine Ecology Progress Series, 598, pp.35-48.

Proud, R., Handegard, N.O., Kloser, R.J., Cox, M.J. and Brierley, A.S., 2019. From siphonophores to deep scattering layers: uncertainty ranges for the estimation of global mesopelagic fish biomass. ICES Journal of Marine Science, 76(3), pp.718-733.

Raclot, T., Groscolas, R. and Cherel, Y., 1998. Fatty acid evidence for the importance of myctophid fish in the diet of king penguins, Aptenodytes patagonicus. Marine Biology, 132, pp.523-533.

Ramsay, J.O. and Silverman, B.W., 2005. Principal components analysis for functional data. Functional data analysis, pp.147-172.

Ramsay J (2024). fda: Functional Data Analysis. R package version 6.2.0, https://CRAN.R-project.org/package=fda.

Reisinger, R.R., Brooks, C.M., Raymond, B., Freer, J.J., Cotté, C., Xavier, J.C., Trathan, P.N., Bornemann, H., Charrassin, J.B., Costa, D.P. and Danis, B., 2022. Predator-derived bioregions in the Southern Ocean: Characteristics, drivers and representation in marine protected areas. Biological Conservation, 272, p.109630.

Saba, G.K., Burd, A.B., Dunne, J.P., Hernández-León, S., Martin, A.H., Rose, K.A., Salisbury, J., Steinberg, D.K., Trueman, C.N., Wilson, R.W. and Wilson, S.E., 2021. Toward a better understanding of fish-based contribution to ocean carbon flux. Limnology and Oceanography, 66(5), pp.1639-1664.

Saenger, R.A., 1989. Bivariate normal swimbladder size allometry models and allometric exponents for 38 mesopelagic swimbladdered fish species commonly found in the North Sargasso Sea. Can. J. Fish. Aquat. Sci. 46, 1986–2002.

Sallée, J.B., 2018. Southern ocean warming. Oceanography, 31(2), pp.52-62.

Sarmiento-Lezcano, A.N., Olivar, M.P., Caballero, M.J., Couret, M., Hernandez-Leon, S., Castellón, A. and Peña, M., 2023. Swimbladder properties of Cyclothone spp. in the northeast Atlantic Ocean and the Western Mediterranean Sea. Frontiers in Marine Science, 10, p.1093982.

Sutton, T.T., Clark, M.R., Dunn, D.C., Halpin, P.N., Rogers, A.D., Guinotte, J., Bograd, S.J., Angel, M.V., Perez, J.A.A., Wishner, K. and Haedrich, R.L., 2017. A global biogeographic classification of the mesopelagic zone. Deep Sea Research Part I: Oceanographic Research Papers, 126, pp.85-102.

R Core Team (2024). _R: A Language and Environment for Statistical Computing_. R Foundation for Statistical Computing, Vienna, Austria. https://www.R-project.org/.

Ryan, T.E., Downie, R.A., Kloser, R.J. and Keith, G., 2015. Reducing bias due to noise and attenuation in open-ocean echo integration data. ICES Journal of Marine Science, 72(8), pp.2482-2493.

Wan, S. and Chen, X., 2024. The spatial distribution and environmental effects on hotspots and coldspots of micronekton in the southwestern Indian Ocean. *Deep Sea Research Part II: Topical Studies in Oceanography*, *214*, p.105367.

Weston, D.E., 1967. Sound propagation in the presence of bladder fish. *Underwater acoustics*, *2*, pp.55-88.

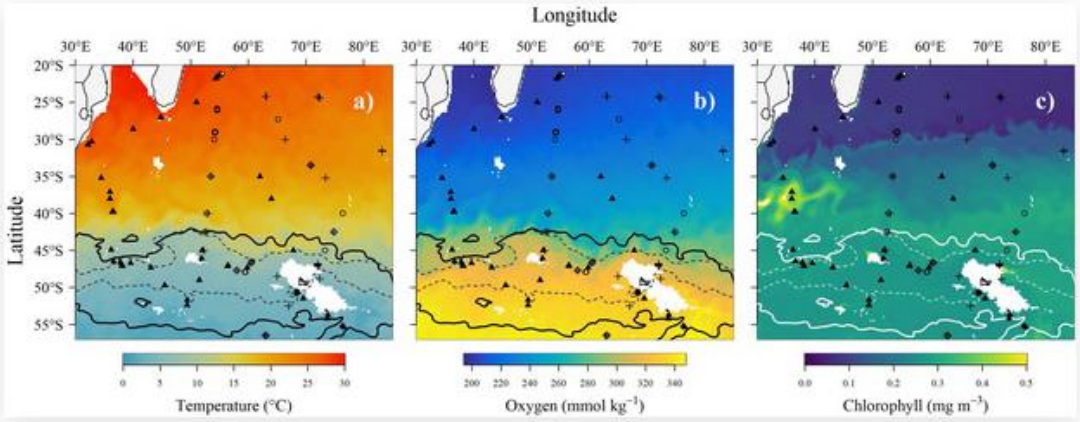

Figure 1. Study area in the southern Indian Ocean showing the monthly averaged sea surface (a) temperature (°C), (b) dissolved oxygen (mmol kg^{-1}), and (c) chlorophyll concentration (mg m^{-3}) in January 2021. Acoustic observations were taken from a set of oceanographic stations conducted across three surveys in 2021 (triangles), 2022 (circles) and 2023 (crosses). Dashed lines indicate the position of the Subantarctic Front and the Polar Front [22]. Solid lines demarcate the weighted 75th percentile of overall habitat importance for marine predators, referred to as Areas of Ecological Significance [23].

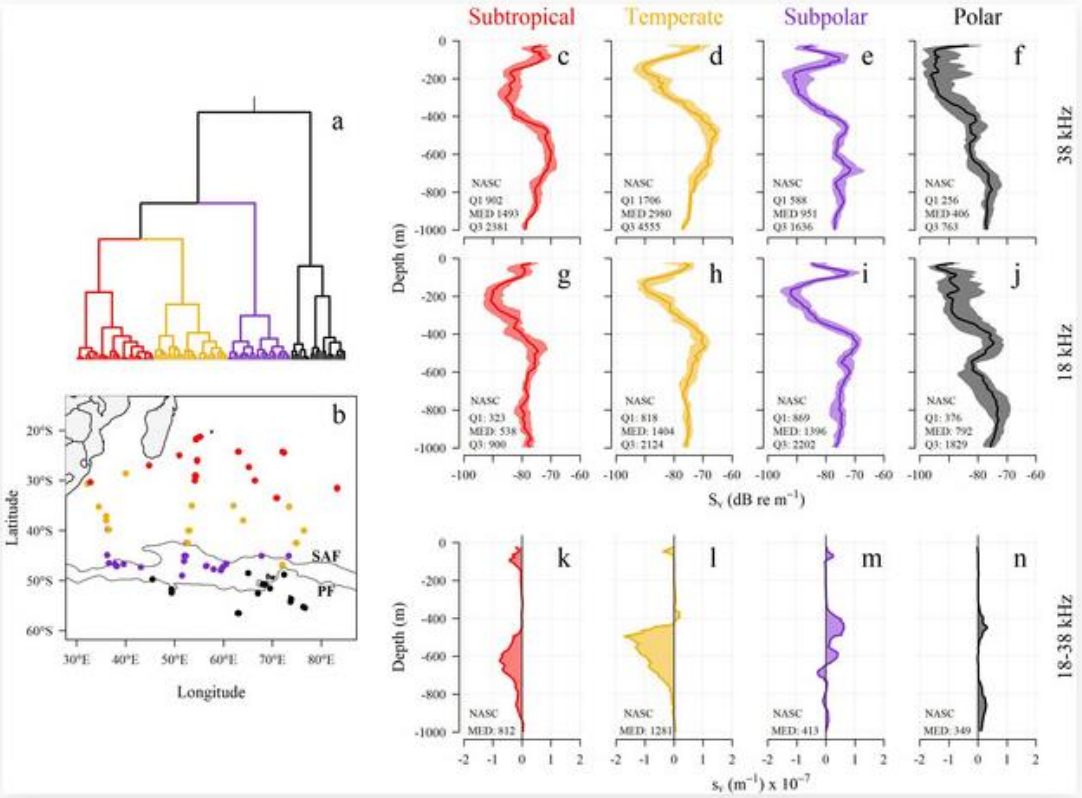

Figure 2. Acoustic seascape classification based on the shape of 38 and 18 kHz daytime profiles, which represents the vertical distribution of sound-scattering fauna. (a) Agglomerative hierarchical clustering shows (b) four classes distributed across latitudinal bands in the southern Indian Ocean. The black lines on the map represent the Subantarctic Front (SAF) and the Polar Front (PF) [22]. Acoustic seascape classes correspond to subtropical (red), temperate (yellow), subpolar (violet) and polar (black) regions. Distinct vertical distributions of sound-scattering fauna are observed across regions at both (c–f) 38 kHz and (g–j) 18 kHz frequencies. In these profiles, the median (solid line) and interquartile ranges (shaded) are depicted. The vertical integration of median and interquartile values is provided at the base of profiles as a proxy of total water-column biomass (NASC, nautical area scattering coefficient, m^2 nmi^{-2}). (k–n) The difference between the 38 and 18 kHz profiles highlights the depths where one frequency dominates the other within each region: positive (negative) values correspond to 18 kHz (38 kHz) dominance.

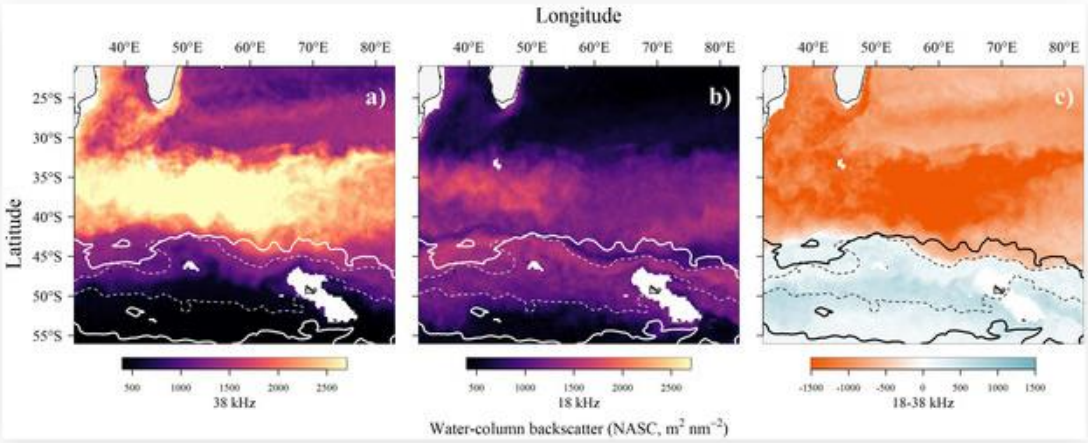

Figure 3. Modelled daytime water-column backscatter (NASC, m^2 nmi^{-2}), a variable often used as a proxy for pelagic fauna density. Backscatter is integrated from 25 to 1000 m depth at (a) 38 kHz, (b) 18 kHz and (c) as the difference of 18 minus 38 kHz. Dotted lines on the map represent the Subantarctic Front and the Polar Front [22]. Solid lines delineate the 75th percentile for Areas of Ecological Significance identified using marine predator trajectories [23]. In (c), note how pelagic fauna changes the frequency response across latitude. North (south) of the subpolar front is dominated by 38 kHz (18 kHz).

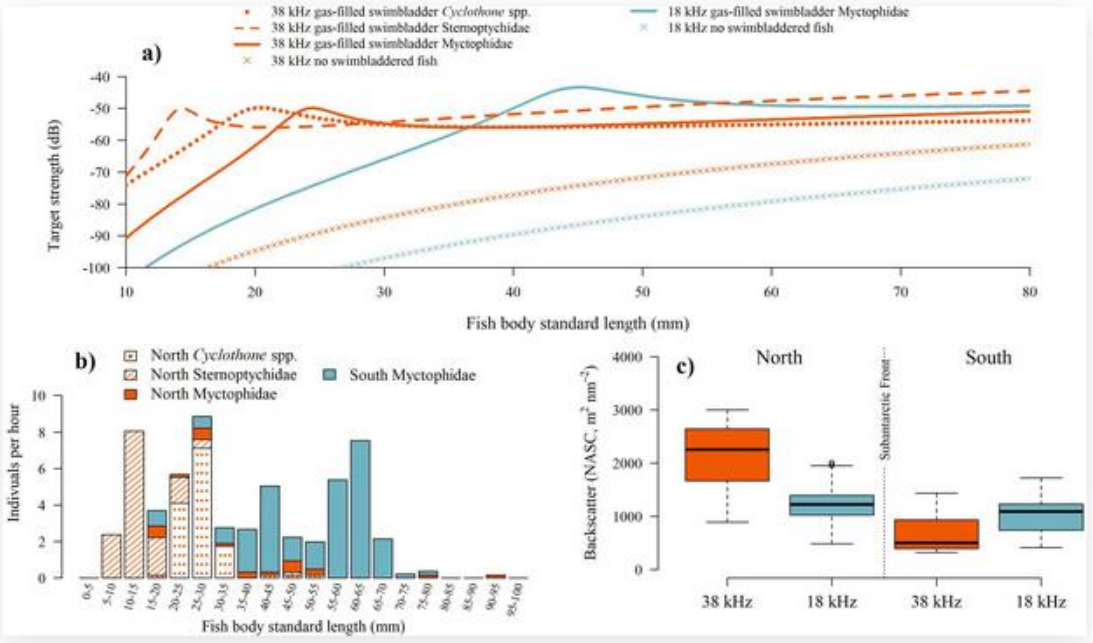

Figure 4. (a) Modelled target strength of *Cyclothone* species (Gonostomatidae), hatchetfish (Sternoptychidae) and lanternfish (Myctophidae) across body lengths of 10–80 mm, assuming a vertical distribution at 500 m depth. The chosen taxa for target strength simulations are based on the occurrence of the main swimbladdered fish species at each side of the Subantarctic Front: *Cyclothone*, Sternoptychidae and Myctophidae in the north, dominated by 38 kHz; Myctophidae in the south, dominated by 18 kHz. (b) Size distribution of the same fish families normalized by sampling effort (individuals per hour) for regions north and south of the Subantarctic Front. (c) Observed daytime water-column backscatter at 38 and 18 kHz, expressed as the nautical area scattering coefficient (NASC, m^2 nmi^{-2}), integrated over depths of 25 to 1000 m. NASC values are shown for regions spanning latitudes from 30° S to 55° S, north and south of the Subantarctic Front.

Supplementary material and results

The following supplementary material provides detailed information on the methodology and intermediate results used to describe and model the vertical distribution of backscatter across the Indian sector of the Southern Ocean, recorded during the *THEMISTO* observation program (DOI 10.18142/288; Table S1). Firstly, we detail the analysis of *in situ* acoustic observations, focusing on the application of functional data analysis and clustering methods. Secondly, the backscatter modelling process using Random Forest with principal components from environmental profiles as predictors is explained. Finally, we describe net sampling methods to validate our acoustic observations, including fishing operations conducted during the 2022 acoustic surveys, as well as historical data from museum collections and literature.

Table S1. Cruises starting and ending dates, and DOI.

Cruise	Starting date	Ending date	DOI
THEMISTO 2021	13/01/2021	08/03/2021	10.17600/18001336
THEMISTO 2022	26/01/2022	06/03/2022	10.17600/18001847
THEMISTO 2023	24/01/2023	28/02/2023	10.17600/18002424

1. Describing *in situ* acoustic observations

The statistical workflow for the first part of our analyses is explained hereafter and visualised in Figure S1.

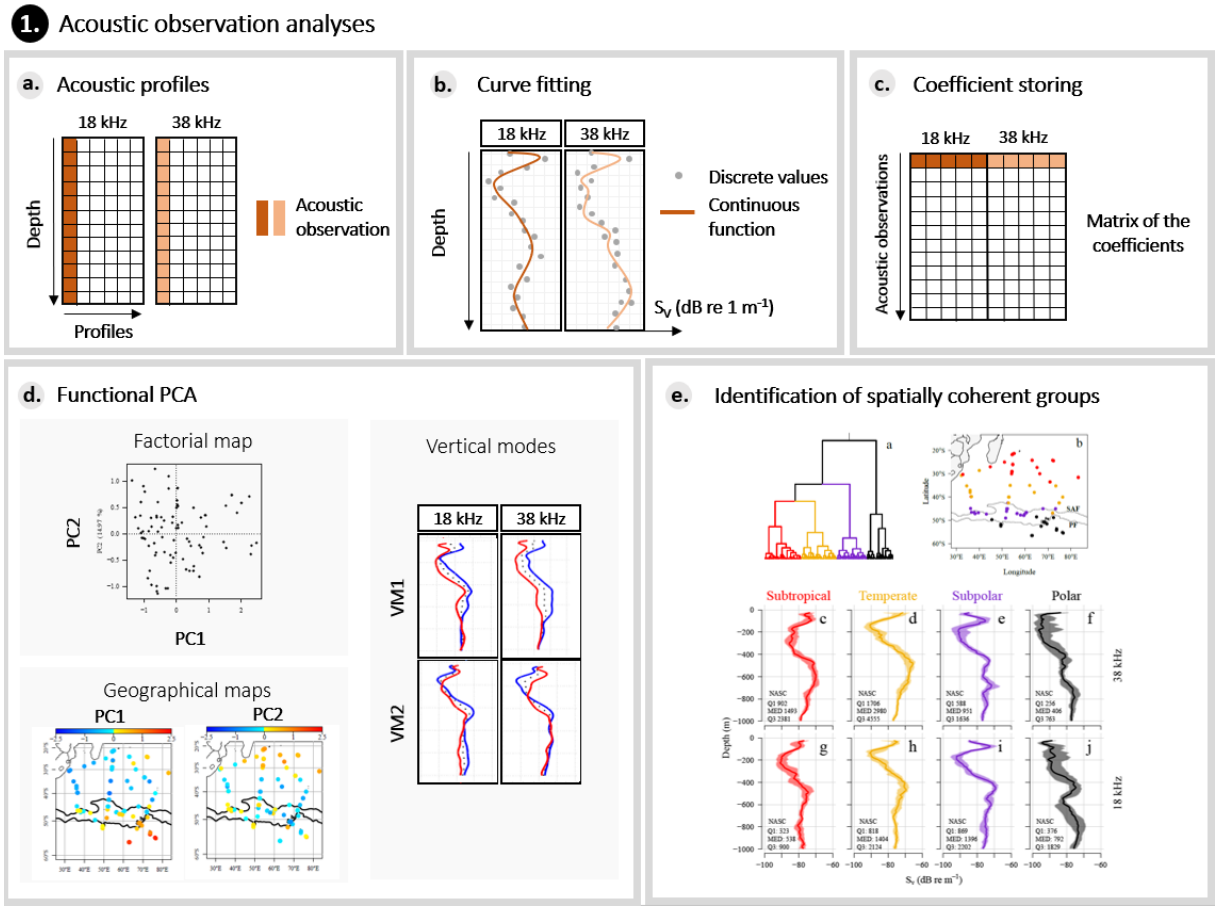

Figure S1. Workflow detailing the analysis of acoustic observations to identify recurring patterns in the vertical distribution of backscatter at 38 and 18 kHz. (a, b) **Smoothing of acoustic profiles**: an acoustic observation is defined as the combination of simultaneously emitted at 38 and 18 kHz. These profiles are smoothed using 25 B-spline basis functions. (c) **Storing of smoothing coefficients**: the smoothing coefficients from both frequencies are stored in a matrix **X**. (d) **Functional Principal Component Analysis (fPCA)**: a multivariate functional Principal Component Analysis is applied to matrix **X**. The resulting principal components (PCs), representing new coordinates of the observations, are visualised on a biplot combining both the principal component space and a geographical map. The associated vertical modes (eigenfunctions) indicate the depth maximising variability. (e) **Clustering of the PCs**: clustering the PCs helps identify groups that are spatially coherent and represent combined vertical structure at both 38 and 18 kHz.

Step a, b – Smoothing of acoustic profiles. The acoustic observations consist of pairs of S_v profiles (38 and 18 kHz) for both daytime and nighttime datasets. Here, we represent the 38 and 18 kHz profiles as a linear combination of 25 B-spline functions to analyse their shape and how they vary together (Figure S2).

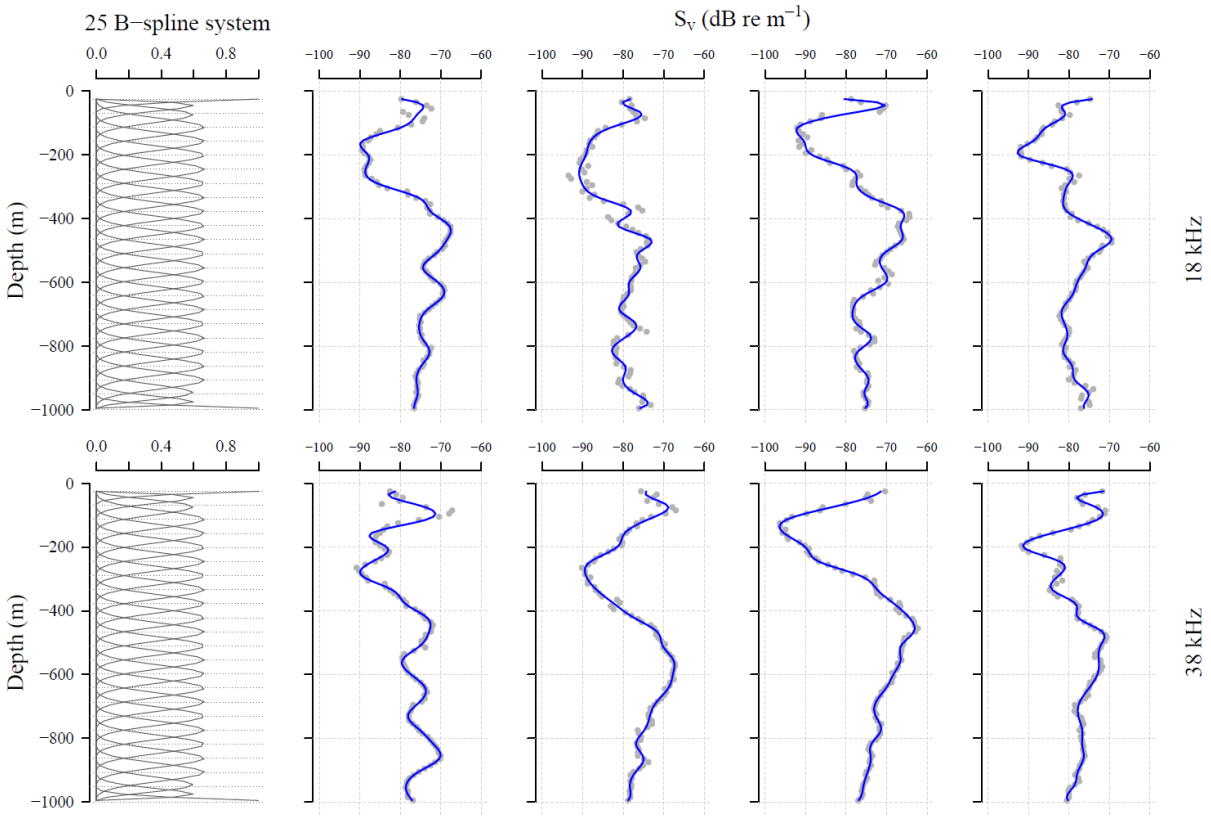

Figure S2. Example of smoothing applied to four acoustic observations from the daytime dataset. The 18 and 38 kHz profiles are smoothed using a 25 B-spline basis system. Grey dots represent the original data, while the blue lines represent the smoothed functional data. Top panels: 18 kHz; Bottom panels: 38 kHz.

To determine the optimal number of spline functions for representing these profiles, we employ the Krzanowski distance method, as described in Godard et al. (2020). These distances are computed using the first 10 principal components, which account for around 90% of the variance. The analysis reveals that using fewer than 25 basis functions would affect the results of the fPCA for daytime observations (Figure S3 top). Selecting 25 basis functions provides a vertical resolution of ~40 m, which is sufficient to resolve backscattering layer thickness and outline the vertical structure of pelagic fauna without overfitting. This choice balances minimising the quadratic error (initial data-to-smoothed data distance) with using a reasonable number of functions (Figure S3 bottom).

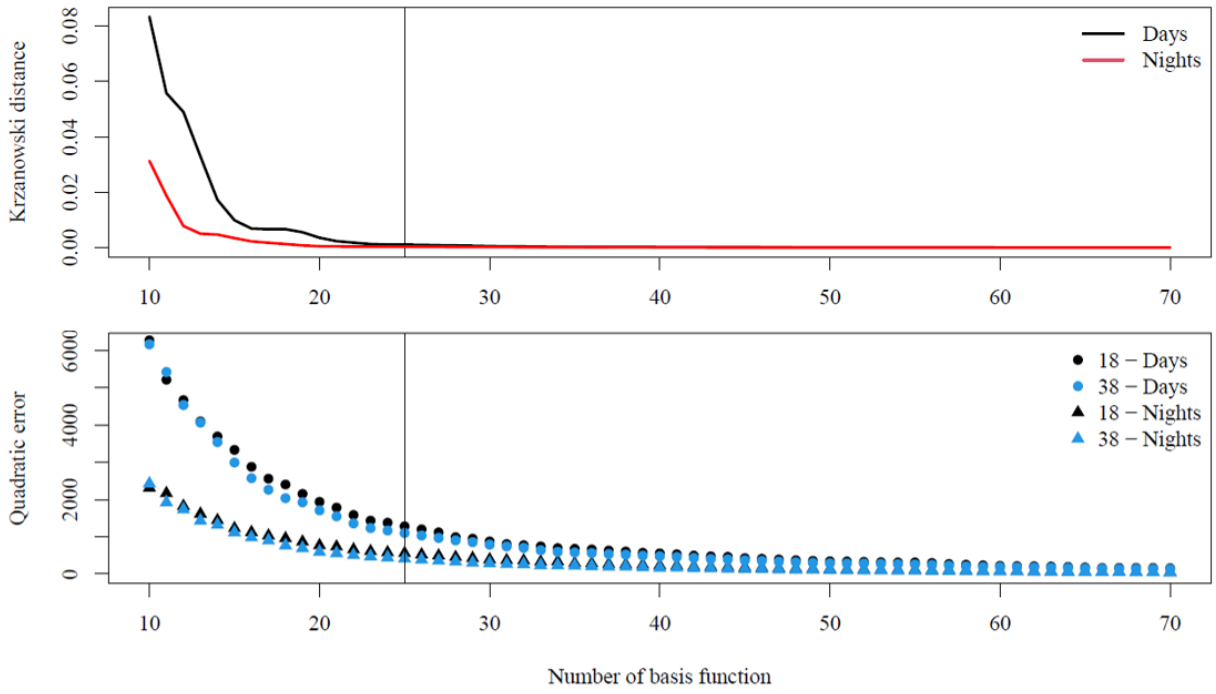

Figure S3. Krzanowski distance (top) and quadratic error (bottom) as a function of the number of basis functions.

Step c, d - Storing of smoothing coefficients and fPCA. We apply functional Principal Component Analysis (fPCA) to capture key patterns in the variability of the smoothed acoustic profiles. The smoothing coefficients from both frequencies (38 and 18 kHz) are concatenated into a single matrix X with dimensions N x 2K, where N represents the number of acoustic observations (ranging from 82 for nighttime to 98 for daytime), and K denotes the number of spline coefficients (identical for both frequencies). The fPCA decomposes this matrix **X** to identify the main modes of variability.

The first four principal components (PCs) explain a substantial portion of the total variance, accounting for 69% and 73% for the daytime and nighttime datasets, respectively. The contribution of each frequency (38 and 18 kHz) to these PCs differs between day and night. During daytime, the first mode is primarily driven by the 38 kHz profile, explaining approximately 65% of the variation in this mode. This contribution decreases to 50% and stabilises around 30% for subsequent modes. At nighttime, the 38 kHz frequency explains approximately 55% of the variance, while the 18 kHz profile dominates the second mode, accounting for about 60% of the variance. Beyond this, the contributions of both frequencies become more similar across subsequent modes.

The principal components analysis results in linearly uncorrelated combinations of the original profiles (38 and 18 kHz), called vertical modes (VMs). These VMs capture the maximum

variance in the data and effectively form a new basis for representing any combination of 38 and 18 kHz profiles. This property is used in Section 2 for further analyses. The PC scores for each observation represent new coordinates in this space, indicating the extent to which a specific acoustic profile aligns with a given VM (Figure S4; Figure S5).

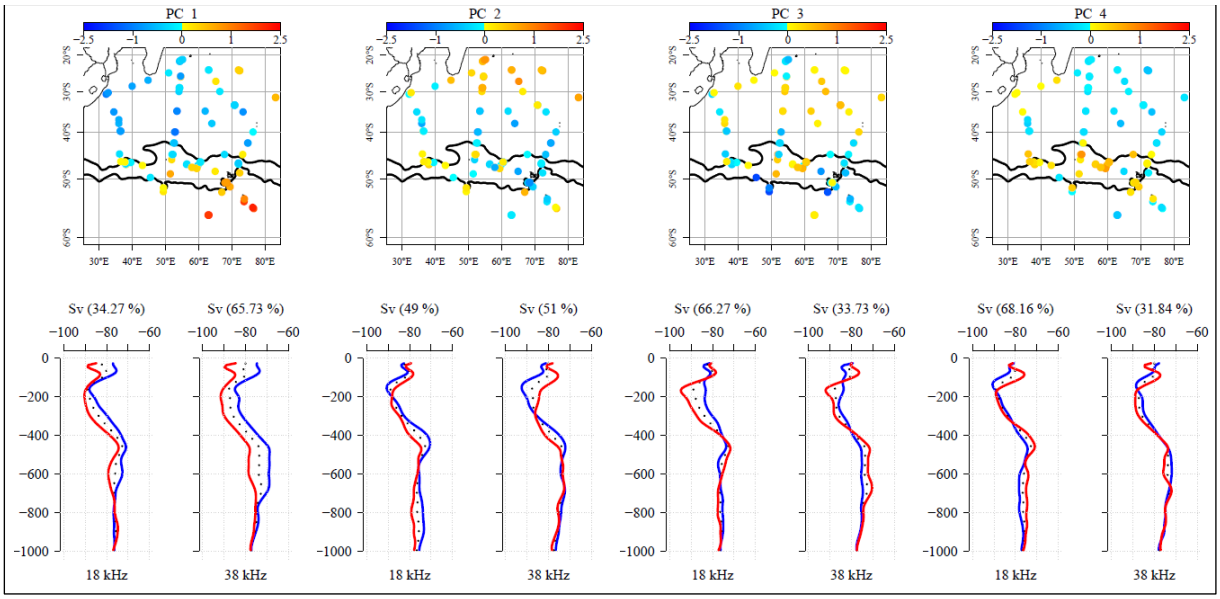

Figure S4. The four principal components (maps) associated with the first four pairs of vertical modes of variability (eigenfunctions) for daytime data.

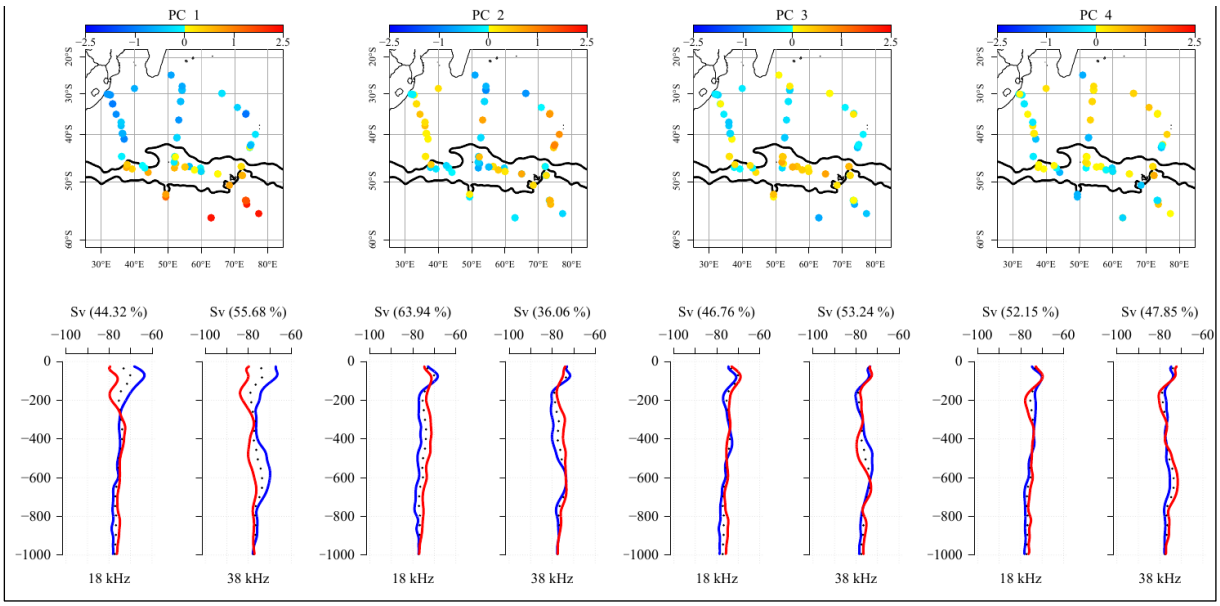

Figure S5. The four principal components (maps) associated with the first four pairs of vertical modes of variability (eigenfunctions) for nighttime data.

Step e - Clustering of the PCs. The final step involves clustering the principal components using agglomerative hierarchical clustering with an ascending approach. This method helps

identify zones with similar vertical distributions of backscatter at both 38 and 18 kHz for daytime (Figure 2) and nighttime (Figure S6) datasets.

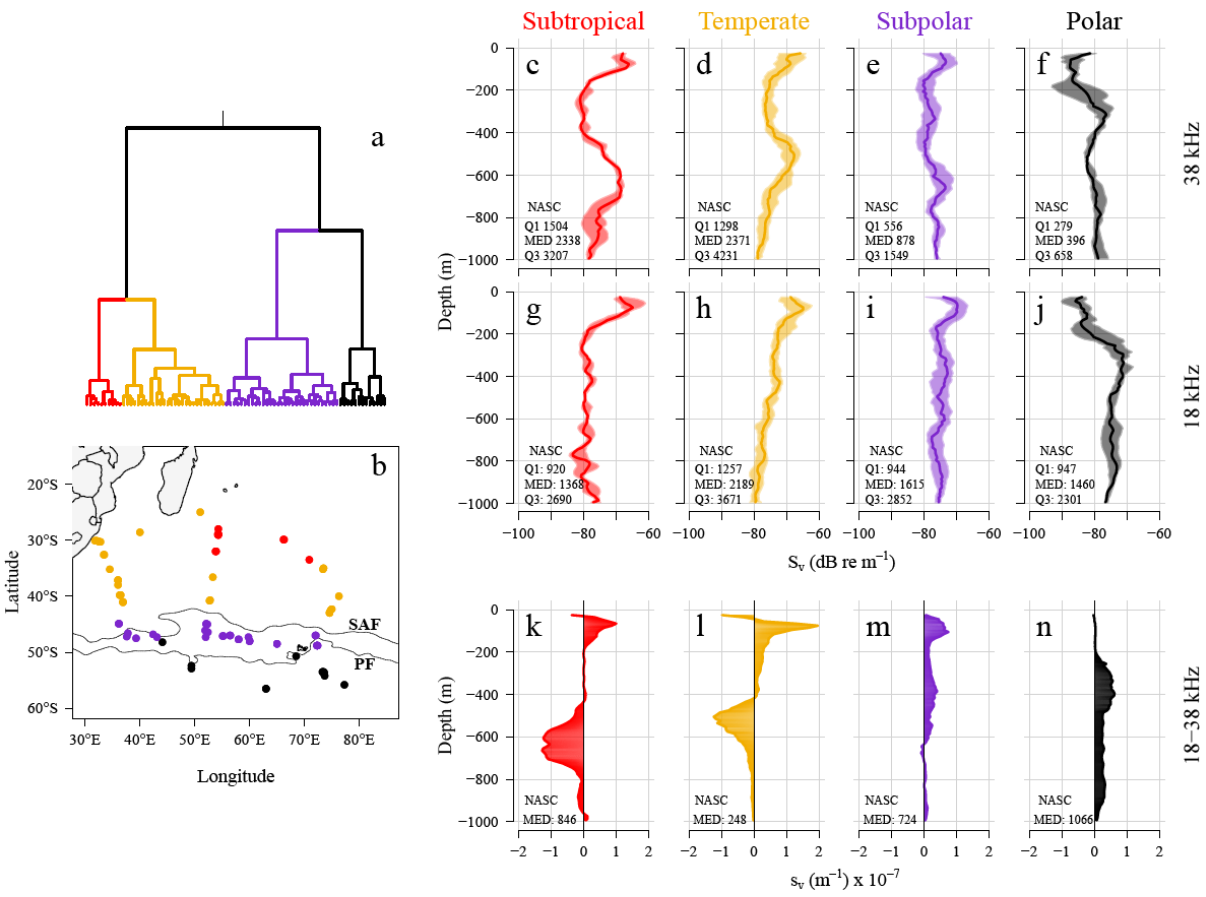

Figure S6. Seascape classification based on the shape of nighttime backscatter profiles at 38 and 18 kHz, representing the vertical distribution of sound-scattering fauna. (a) Agglomerative hierarchical clustering results in (b) four seascape classes distributed across latitudinal bands in the Southern Indian Ocean. The black lines on the map represent the Subantarctic Front and the Polar Front (Park et al. 2019). Seascape classes are assigned for subtropical (red), temperate (yellow), subpolar (violet) and polar (black) regions. Distinct vertical distributions of sound-scattering fauna are observed across these regions at both (c-f) 38 kHz and (g-j) 18 kHz frequencies. In these profiles, the median (solid line) and interquartile ranges (shaded) are depicted. At the base of these profiles, the vertical integration of median and interquartile values is provided as a proxy of total water column biomass (NASC: Nautical Area Scattering Coefficient, m^2 nmi^{-2}). (k-n) Frequency-dependent differences in backscatter highlight the depths where one frequency dominates the other: positive (negative) values indicate greater backscatter at 18 kHz (38 kHz) within each region.

To complement the clustering analysis, we computed additional metrics based on the smoothed profiles (expressed as medians), following the terminology defined by MacLennan et al. (2002). The volume backscattering coefficient (s_v) is obtained by converting the smoothed profiles from volume backscattering strength (S_v, dB re 1 m^{-1}). The integrated Nautical Area Scattering Coefficient (NASC) is calculated from the S_v profiles and displayed at the bottom of each profile. This NASC value serves as a proxy for the total acoustic biomass integrated within the water column.

$$s_v = 10^{(S_v/10)} \qquad (\mathrm{m}^{-1}) \qquad (1)$$

$$s_a = \int_{-1000}^{-25} s_v \, dz \qquad (\mathrm{m}^2\mathrm{m}^{-2}) \qquad (2)$$

$$NASC = 4\pi(1852)^2 s_a \qquad (\mathrm{m}^2\mathrm{nmi}^{-2}) \qquad (3)$$

2. Extending *in situ* observation to regional acoustic seascapes

The statistical workflow for the second part of our analyses is detailed hereafter and visualised in Figure S7. Step 2a. follows Step 1d.

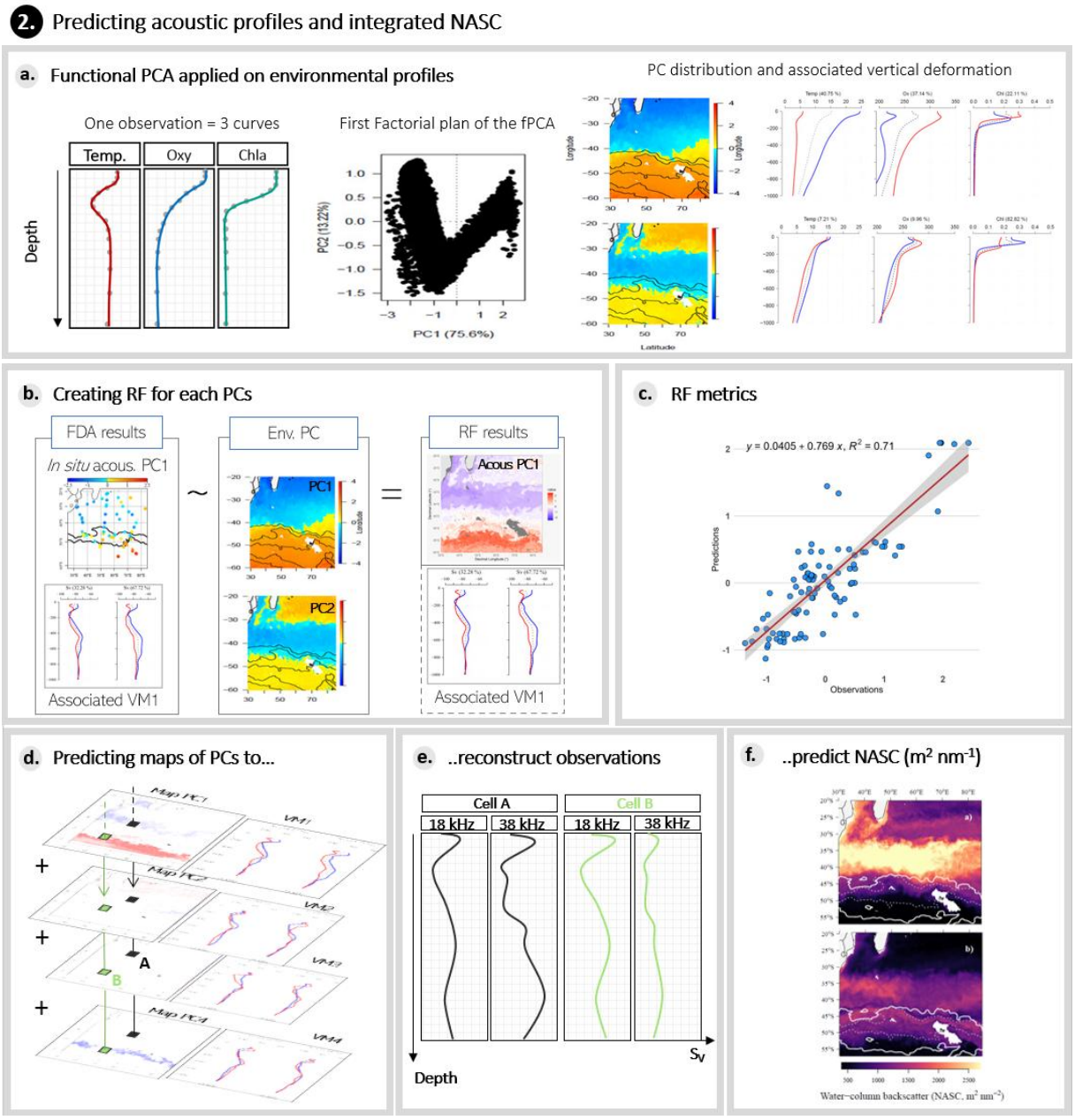

Figure S7. Workflow for extending clusters to acoustic seascapes. (a) **Decomposition of environmental variables**: an fPCA is applied to temperature, oxygen, and chlorophyll-a profiles. (b) **Modelling Principal Components** (PCs): each PC, representing a mode of variability in backscatter profiles, is modelled independently using the first two environmental PCs as predictors. (c) **Model evaluation**: the performance of each model in predicting a PC is assessed. (d) **Predicting vertical structure**: the modelling process yields a series of predicted PCs associated with vertical modes of variability. (e) **Reconstructing acoustic observations**: we use the linear combination of the predicted PCs and their associated eigenfunctions to reconstruct acoustic observation in S_v. (f) **Estimating acoustic biomass**: each predicted S_v profile is converted into NASC to investigate spatial patterns of integrated biomass across the seascape.

We use Random Forest models to extend the analysis beyond the identified clusters across the region. This method involves modelling each principal component as a function of environmental variables, including temperature, chlorophyll-a, and oxygen profiles from the surface to 1000 m depth (Figure S8). Environmental data were sourced from the E.U. Copernicus Marine Service Information. Temperature profiles were obtained from the Global Ocean Physics Reanalysis (1/12°; 10.48670/moi-00021), while chlorophyll and dissolved oxygen profiles were retrieved from the Global Ocean Biogeochemistry Analysis and Forecast (1/4°; 10.48670/moi-00015).

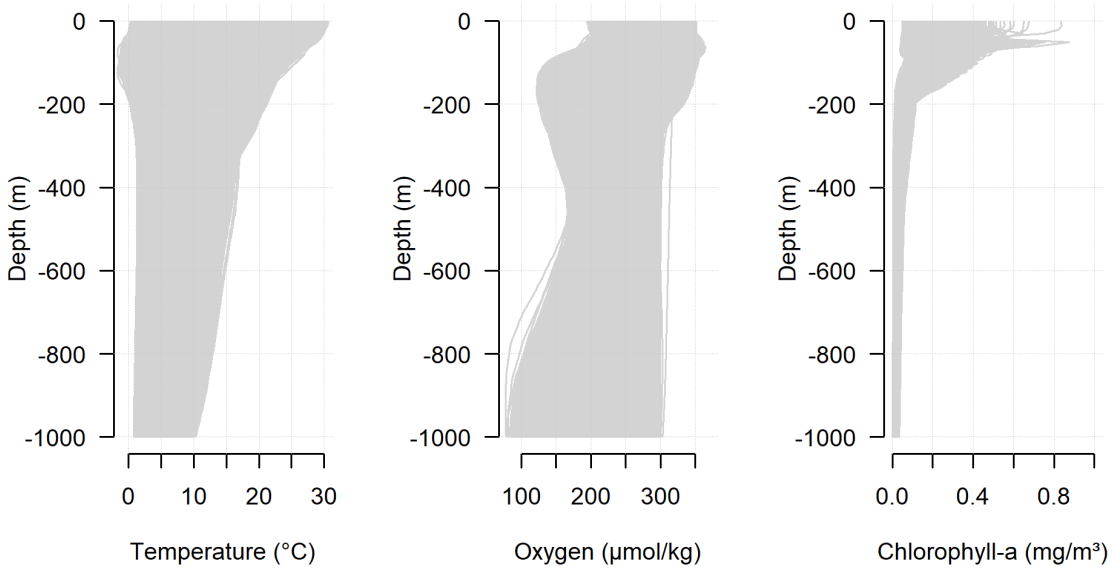

Figure S8. Temperature, oxygen, and chlorophyll profiles representing the 3-D variability of the environmental system in the study area. Surface data points from January 2021 are displayed in Figure 1 of the manuscript.

Step a – Decomposing environmental profiles

The first step of this analysis is to reduce the dimensionality of the environmental system. Like the active acoustic profile analysis, we defined one environmental observation as the simultaneous profiles of temperature, chlorophyll-a and oxygen. We smoothed the data (Figure S9) using 50 basis functions (with penalisation $\lambda = 0.05$), followed by a functional Principal Component Analysis (fPCA) to reduce the initial variability of the system. The fPCA was conducted on monthly profiles from January to March, from 2021 to 2023.

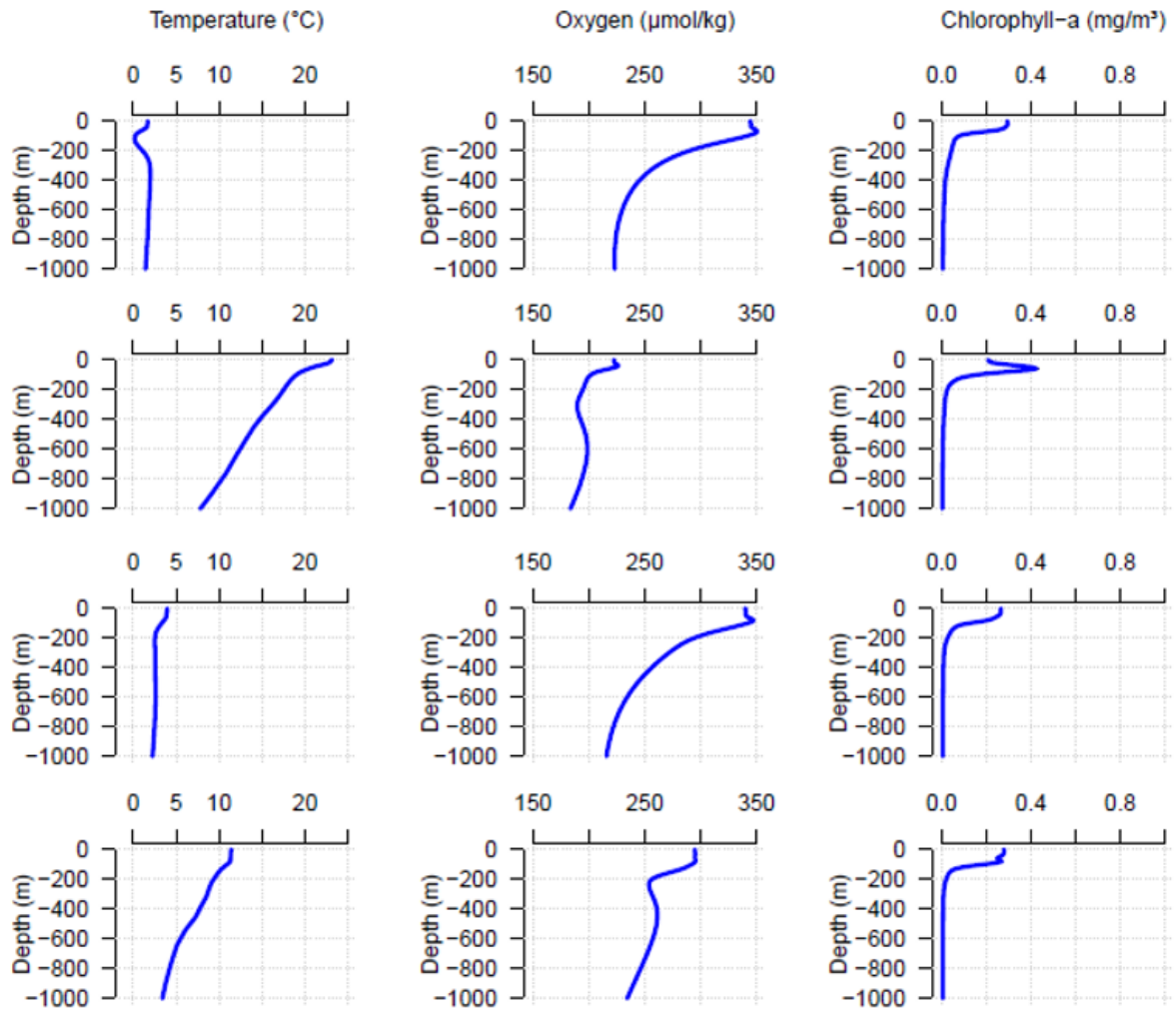

Figure S9. Smoothed environmental profiles for four different observations (rows).

We retained two principal components, capturing ~90% of the variance as supported by the broken-stick method. The first mode was primarily driven by temperature and oxygen, while the second was influenced by chlorophyll-a (Figure S10).

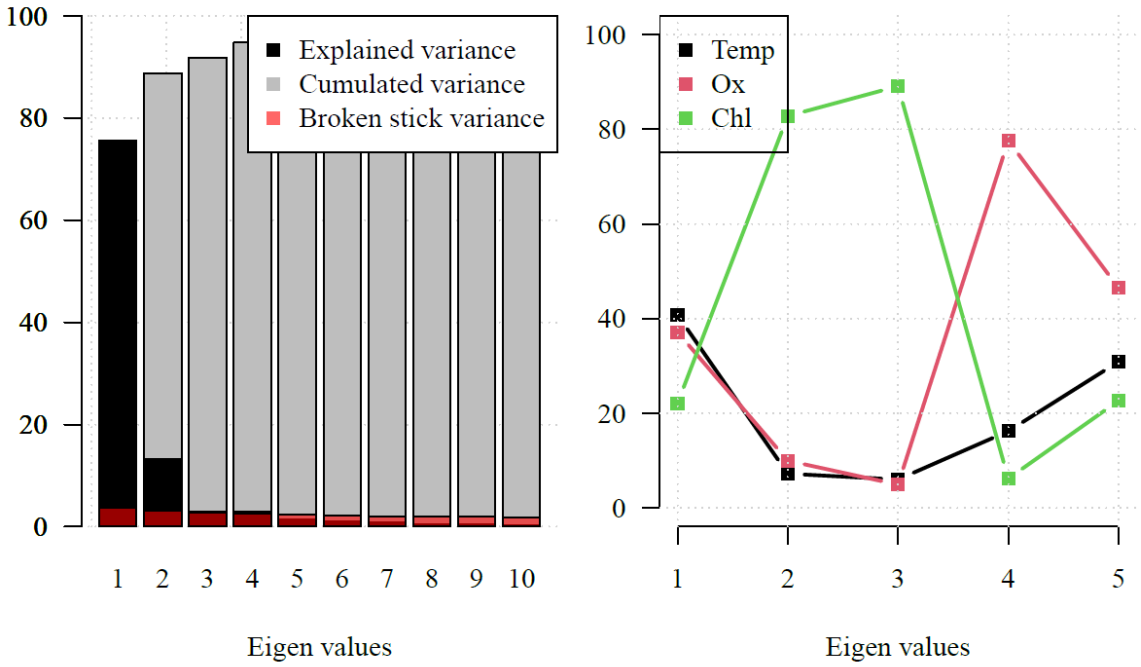

Figure S10. Distribution of inertia across eigenvalues and the contribution of the frequencies to each eigenvalue.

Visualising the PC per period resulted in 9 * 2 maps: 9 periods (January, February, and March of 2021 2022, and 2023) for PCs 1 and 2. Figure S11 shows the first and second factorial planes, as well as the spatial projection of PCs 1 and 2 for January 2021.

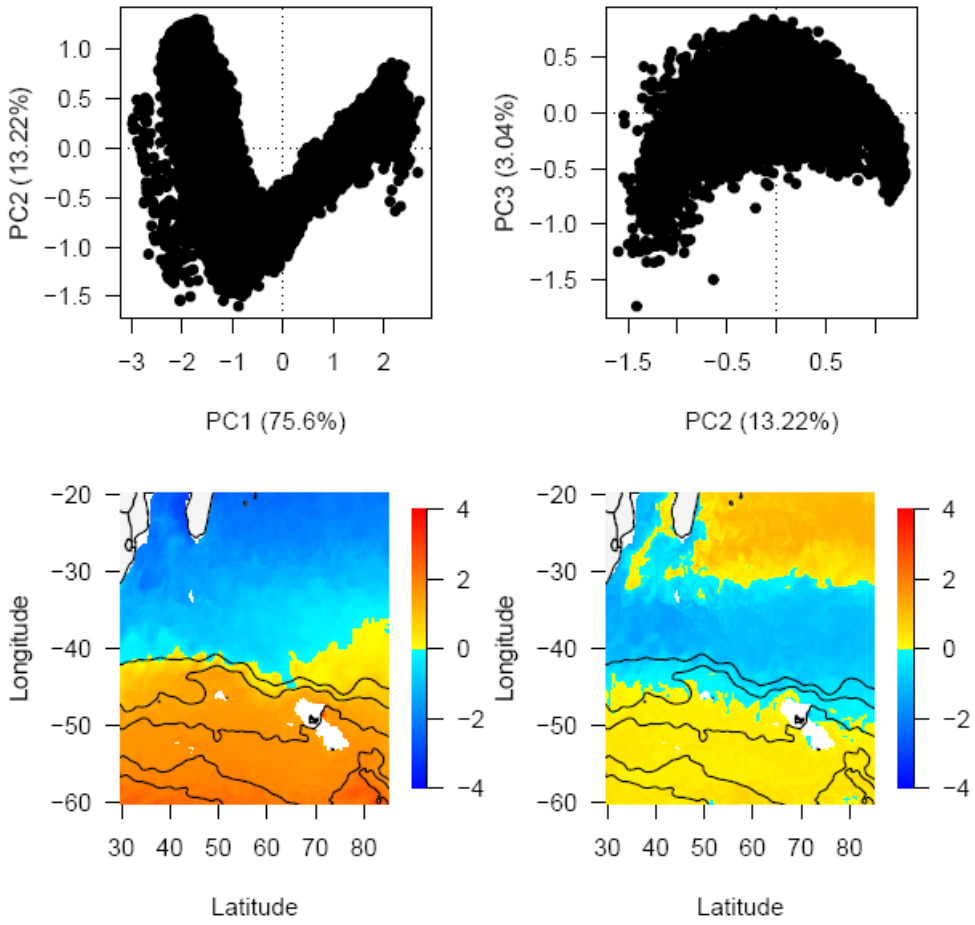

Figure S11. First and second factorial planes (top), and corresponding values (PC1 and PC2) projected onto a map (bottom) for January 2021.

The vertical deformation associated with the principal components, the eigenfunctions of the system, is shown in Figure S12.

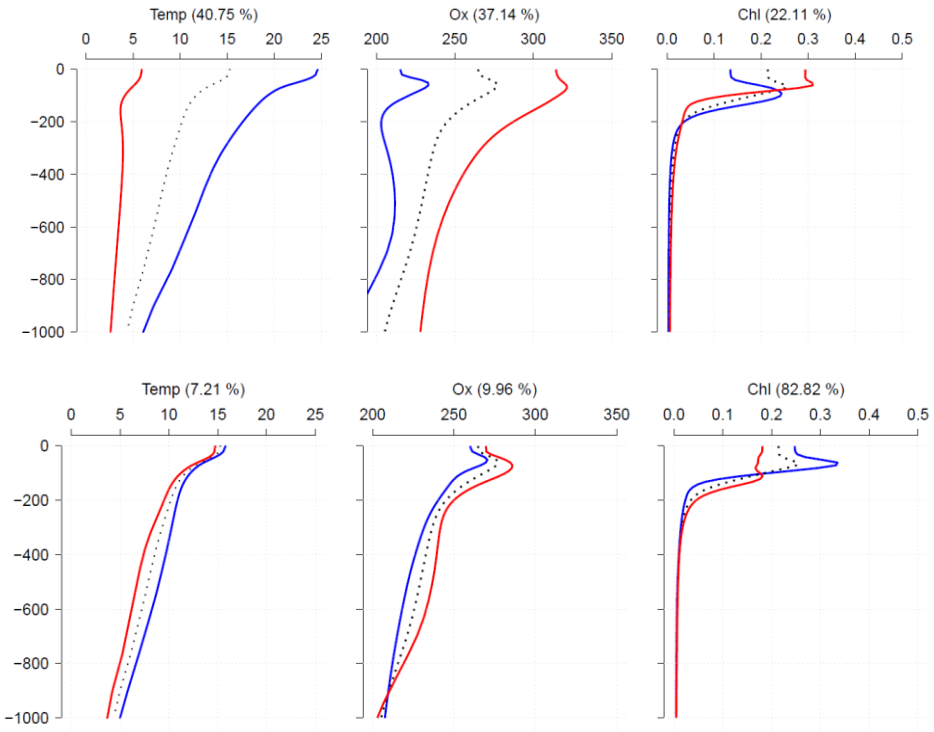

Figure S12. Eigenfunctions of the system for each environmental variable, associated with the first (top) and second (bottom) eigenvalues.

To use these environmental principal component maps for predicting acoustic backscatter, we matched daily environmental profiles (from the same datasets) to each acoustic observation (Figure S13).

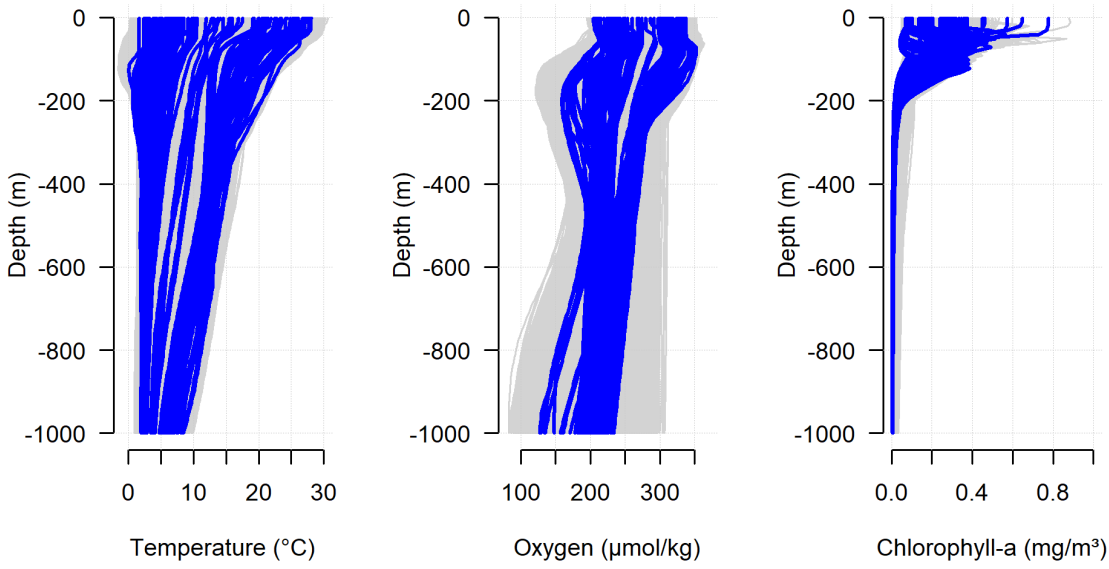

Figure S13. Monthly (grey) and daily (blue) profiles associated with the acoustic observations.

Once matching was completed, we projected the daily profiles onto the fPCA space derived from the monthly environmental analysis, allowing us to compute principal component for these profiles (Figure S14).

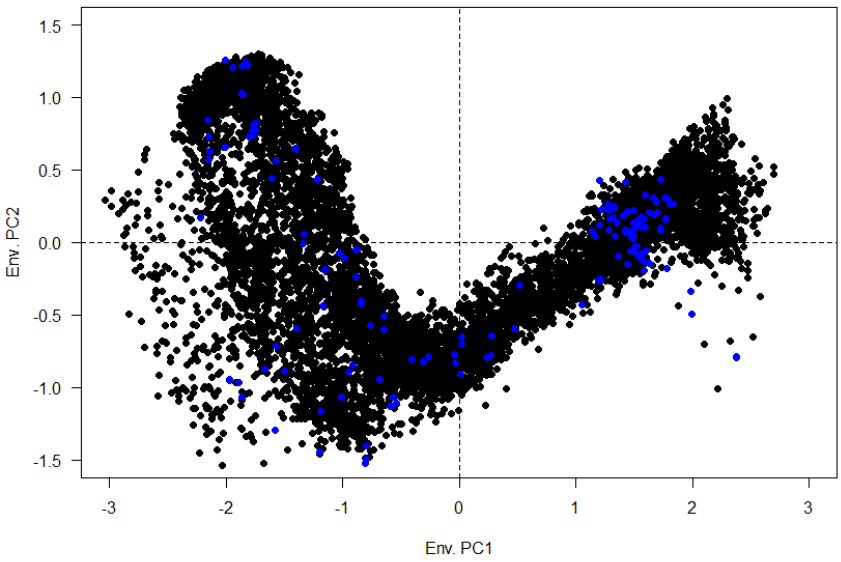

Figure S14. Projection of daily profiles (blue points) onto the first factorial plan of the fPCA computed on the monthly profiles (black points).

Step b - Modelling Principal Components. We build a separate model for each acoustic PC, trained on the daily environmental PC scores, to predict spatial distributions across the study area and for each period. This allows us to map the predicted values for each acoustic PC, revealing large-scale spatial patterns associated with the original backscatter signals captured by the PCs. It is important to note that this modelling process focuses solely on the PCs, leaving the underlying vertical modes (eigenfunctions) unchanged. These eigenfunctions serve as the basis for reconstructing the acoustic observations in later steps.

Step c - Model evaluation. Random Forest predictions are generated for each principal component in both daytime and nighttime datasets, resulting in a total of eight models (4 PCs per period). To ensure model robustness and prevent overfitting, we implement a hyperparameter tuning strategy. Specifically, a hyperparameter grid search is conducted to optimise five key hyperparameters:

1. **The number of trees** balances error stability with computational efficiency.
2. **The number of variables** randomly sampled at each split.
3. **The number of samples** used for training. By default, this corresponds to 63.25% of the training dataset to reflect the expected number of unique observations in a bootstrap sample. Deviating from this value can influence training time and introduce varying levels of bias.
4. **The minimum number of samples within terminal nodes** influences tree complexity, depth, and intricacy. Smaller node sizes yield deeper and more complex trees, while larger

node sizes lead to shallower trees. This involves a trade-off between bias and variance: deeper trees may introduce more variance (risk of overfitting), whereas shallower trees may increase bias.

5. **The maximum number of terminal nodes** offers another way to manage tree complexity. More nodes result in deeper, more complex trees, while fewer nodes lead to shallower trees.

To optimise these parameters, and therefore to ensure model robustness and prevent overfitting, we use the "RandomDiscrete" method in the R package h2o, which randomly samples different hyperparameter settings. In our case, the total number of tested combinations is 7200 (20*3*5*6*4), based on:

- Number of trees in the forest (=20)
- Number of variables considered at each split (=3)
- Proportion of samples used for training (=5)
- Minimum number of samples in terminal nodes (=6)
- Maximum number of terminal nodes (=4)

The search process stops when a predefined stopping criterion is met, such as a significant improvement in model performance, reaching a time limit, or evaluating a specified number of models. Here, we consider all three criteria to identify the best models for each principal component.

Model performance is evaluated using Out-of-Bag Root Mean Squared Error (OOB RMSE). While random search does not guarantee the absolute optimal model, it is effective in finding models with minimal OOB RMSE. Additionally, we calculate mean residual deviance, mean absolute error (MAE), and R-squared to assess the overall quality of the models (Table S2).

Once the best models are identified for each PC in both daytime and nighttime datasets, we use them to predict the spatial distribution of PCs across the entire study area based on monthly environmental PCs for a given period (e.g., environmental PC 1 and 2 for January 2021). Finally, we evaluate the agreement between the original and model-predicted PC values using the Pearson correlation coefficient.

Table S2. Performance evaluation of Random Forest models for each acoustic principal component (PC) for both daytime and nighttime datasets. RMSE: Root Mean Squared Error. MAE: Mean Absolute Error. R-squared: Coefficient of determination. p: pvalue.

		Day				**Night**			
		PC1	**PC2**	**PC3**	**PC4**	**PC1**	**PC2**	**PC3**	**PC4**
Hyperparameter values	Number of trees	50	44	38	21	50	44	38	21
	Number of variables sampled at each split	1	1	2	2	1	1	2	2
	Number of samples used for training	0.7	0.7	0.7	0.632	0.7	0.7	0.7	0.632
	Minimum number of samples within terminal nodes	1	1	1	3	1	1	1	3
	Maximum number of terminal nodes	10	20	5	5	10	20	5	5
(Mean) Metric of evaluation	RMSE	0.390	0.344	0.445	0.273	0.395	0.390	0.288	0.283
	Mean residual deviance	0.163	0.173	0.230	0.09	0.161	0.159	0.09	0.09
	MAE	0.317	0.284	0.344	0.211	0.318	0.310	0.225	0.222
	R-squared	0.692	0.539	0.239	0.578	0.717	0.437	0.428	0.225
	Pearson correlation between observed and modelled PC	0.92 p <0.001	0.83 p<0.001	0.74 p<0.001	0.83 p<0.001	0.91 p<0.001	0.73 p<0.001	0.8 p<0.001	0.61 p<0.001

The relative influence of each environmental variable on the predicted PCs is assessed for both daytime and nighttime datasets. We consider two key metrics:

(i) the frequency of selection, indicating how often a variable is chosen to split the data during tree construction in the Random Forest models.

(ii) the error reduction to assess the extent to which a variable contributes to reducing the squared error across all the trees in the forest.

Env. PC1 (driven by the vertical distribution of oxygen and temperature) emerges as the most influential variable for predicting daytime acoustic PCs, contributing consistently around 50-60% to the first three acoustic PCs and increasing to 90% for PC4. At nighttime, its influence is dominant for acoustic PC1 (80%) and moderate for PC3 and PC4 (~50%). In contrast, Env. PC2 (driven by the vertical distribution of chlorophyll-a) plays a primary role (~95%) in explaining acoustic PC2 (Figure S8).

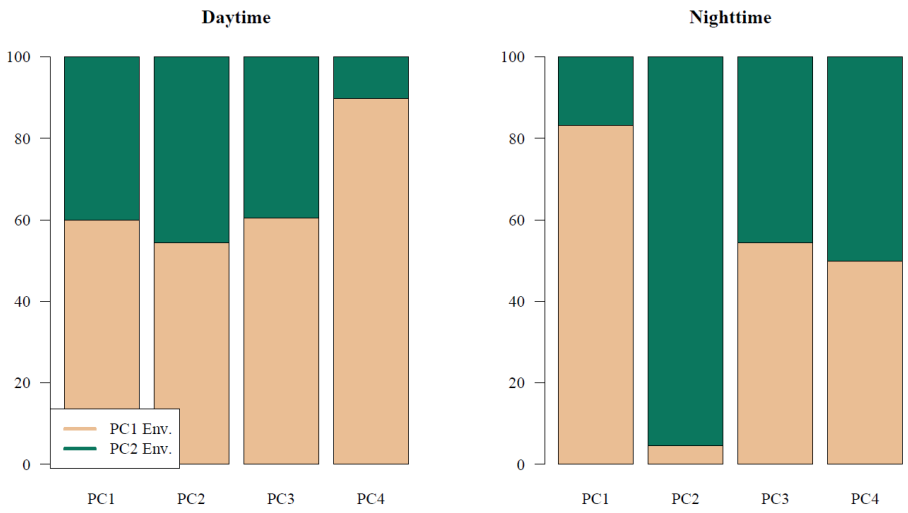

Figure S15. Percentage contribution of the first two principal components (PCs) derived from the original environmental variables, used to model the first four principal components of acoustic data. Results are shown for daytime (left panel) and nighttime (right panel).

Step d - Predicting vertical structure. Steps 2a and 2b culminate in a series of eight maps for each period (January, February, and March of 2021, 2022, and 2023), representing each PC in both daytime and nighttime datasets (Figure S10). Each map corresponds to a specific vertical backscatter pattern, as depicted in Figure S5. For instance, the first PC map (both in daytime and nighttime) reflects the latitudinal variation in the vertical distribution of organisms south of the Subantarctic Front. Other PCs, such as PC4 for daytime and PC3 for nighttime, capture more localised patterns, particularly around the subantarctic islands.

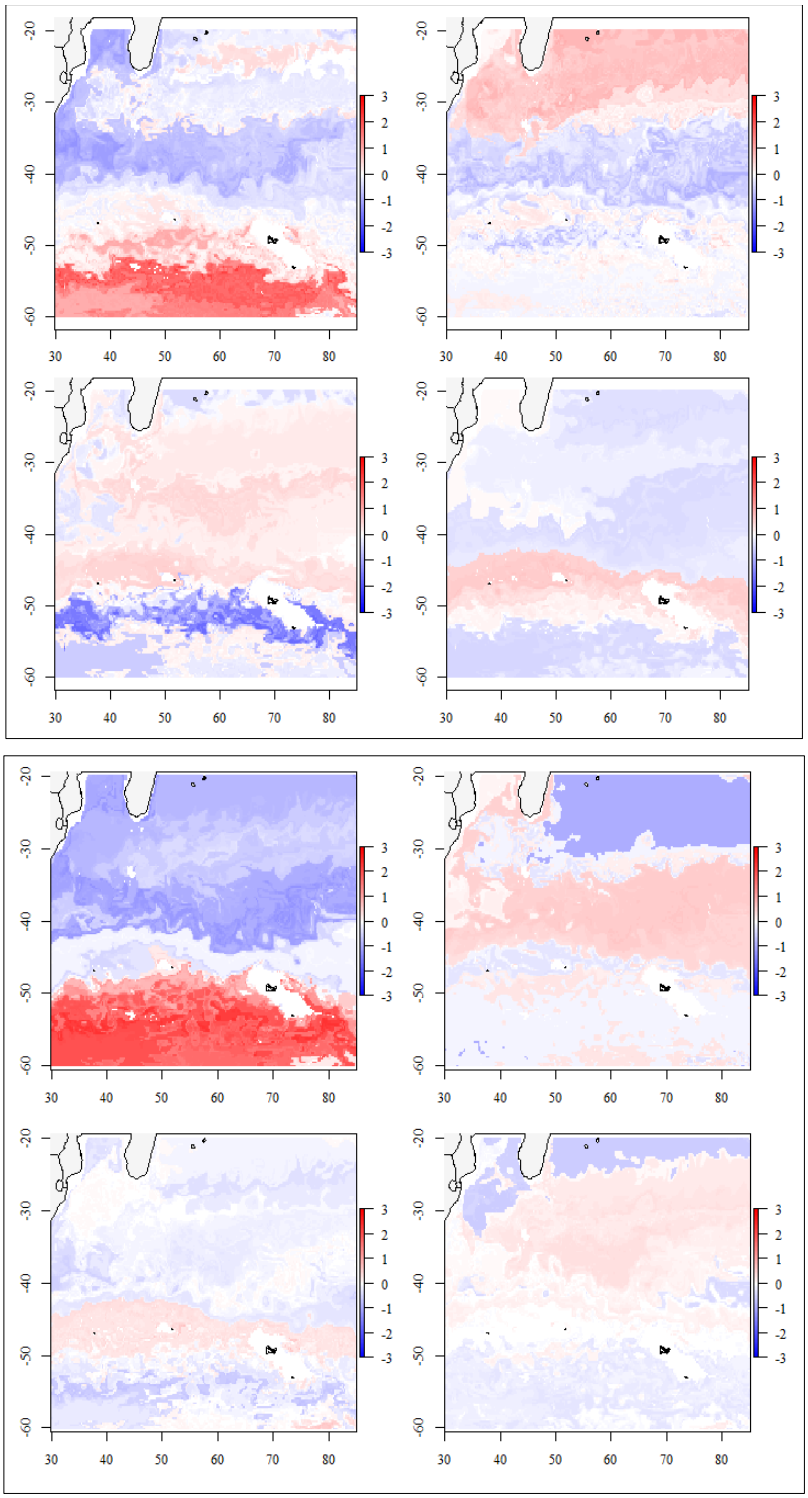

Figure S16. Predicted principal component scores from the Random Forest models for January 2021. Daytime (top panels) and nighttime (bottom panels).

Uncertainty in the correlation estimates is represented by 95% confidence intervals, reflecting the precision of the relationships between the predicted mean principal components and their observed counterparts (Figure S17). The Pearson correlation coefficients are as follows:

Mean PC1 vs A_CP1: r = 0.88 (95% CI: 0.83, 0.92), p < 0.001

Mean PC2 vs A_CP2: r = 0.79 (95% CI: 0.7, 0.86), p < 0.001

Mean PC3 vs A_CP3: r = 0.56 (95% CI: 0.41, 0.68), p < 0.001

Mean PC4 vs A_CP4: r = 0.82 (95% CI: 0.75, 0.88), p < 0.001

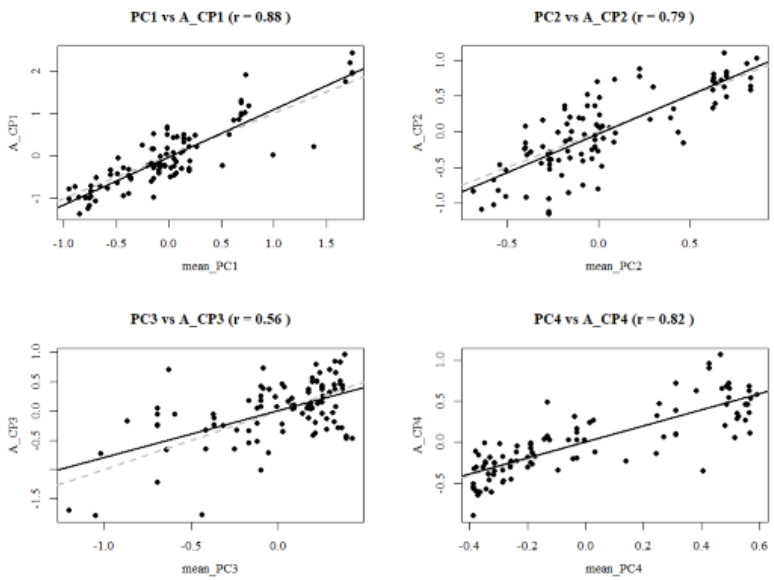

Figure S17. Pairwise scatter plots comparing the predicted mean principal components (PC1 to PC4) with the observed acoustic principal components (A_CP1 to A_CP4) at the same spatial locations. Each panel shows the 1:1 line (dashed grey) and the linear regression line (solid black). The corresponding correlation coefficient (Pearson's r) is indicated in the title of each plot.

Step e - Reconstructing acoustic observations. Using the predicted PC maps and the previously identified vertical modes (VMs; Figure S7a), we reconstruct acoustic observations for any grid cell within the study area. This reconstruction follows the notation by Pauthenet et al. (2018):

$$\begin{cases} P18_n^{(q)}(z) = \overline{P18}(z) + \sum_{k=1}^{q} y_{n,k}\xi_k^{P18}(z) \\ P38_n^{(q)}(z) = \overline{P38}(z) + \sum_{k=1}^{q} y_{n,k}\xi_k^{P38}(z) \end{cases} \quad (4)$$

where q=4 (number of principal components used); n = 1, …, N (number of observations); k = 1, …, 4 (mode number); z the depth in m (z ∈ 25-1000), ξ refers to the eigenfunctions, y denotes the principal component scores and $\overline{P_{38}}(z)$ and $\overline{P_{18}}(z)$ correspond to the mean acoustic profiles at 38 kHz and 18 kHz, respectively.

To evaluate the accuracy of the reconstruction, we compare the observed 38 kHz and 18 kHz acoustic profiles with the predicted mean profiles of identified echobiomes (Figure S18).

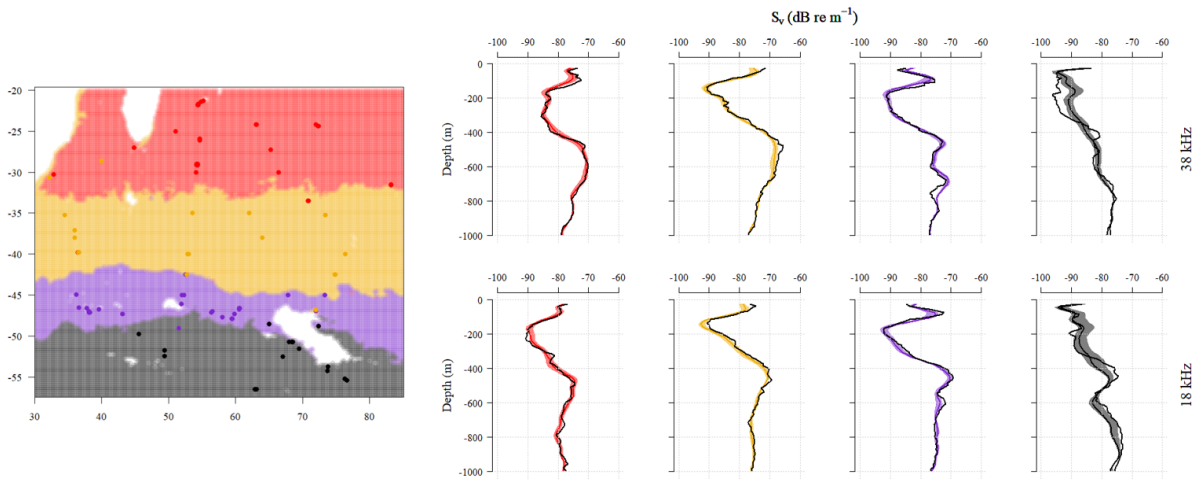

Figure S18. Predicted versus observed acoustic profiles. In colour, mean acoustic profiles at 38 and 18 kHz (± interquartile range Q1–Q3) associated with the predicted echobiomes. The black curves indicate the mean observed acoustic profiles associated with each echobiome. The map (left panel) shows the geographical distribution of acoustic observations (points) and their associated predicted echobiomes (coloured areas).

Step f – Integrated backscatter. Following the reconstruction of each acoustic observation, each predicted S_v profile at 38 and 18 kHz is converted to NASC using Equations 1 and 2. This conversion enables a detailed analysis of spatial patterns in integrated backscatter distribution and their temporal variability across different periods (Figure S19). The difference in NASC between the two frequencies highlights changes in acoustic dominance across different locations.

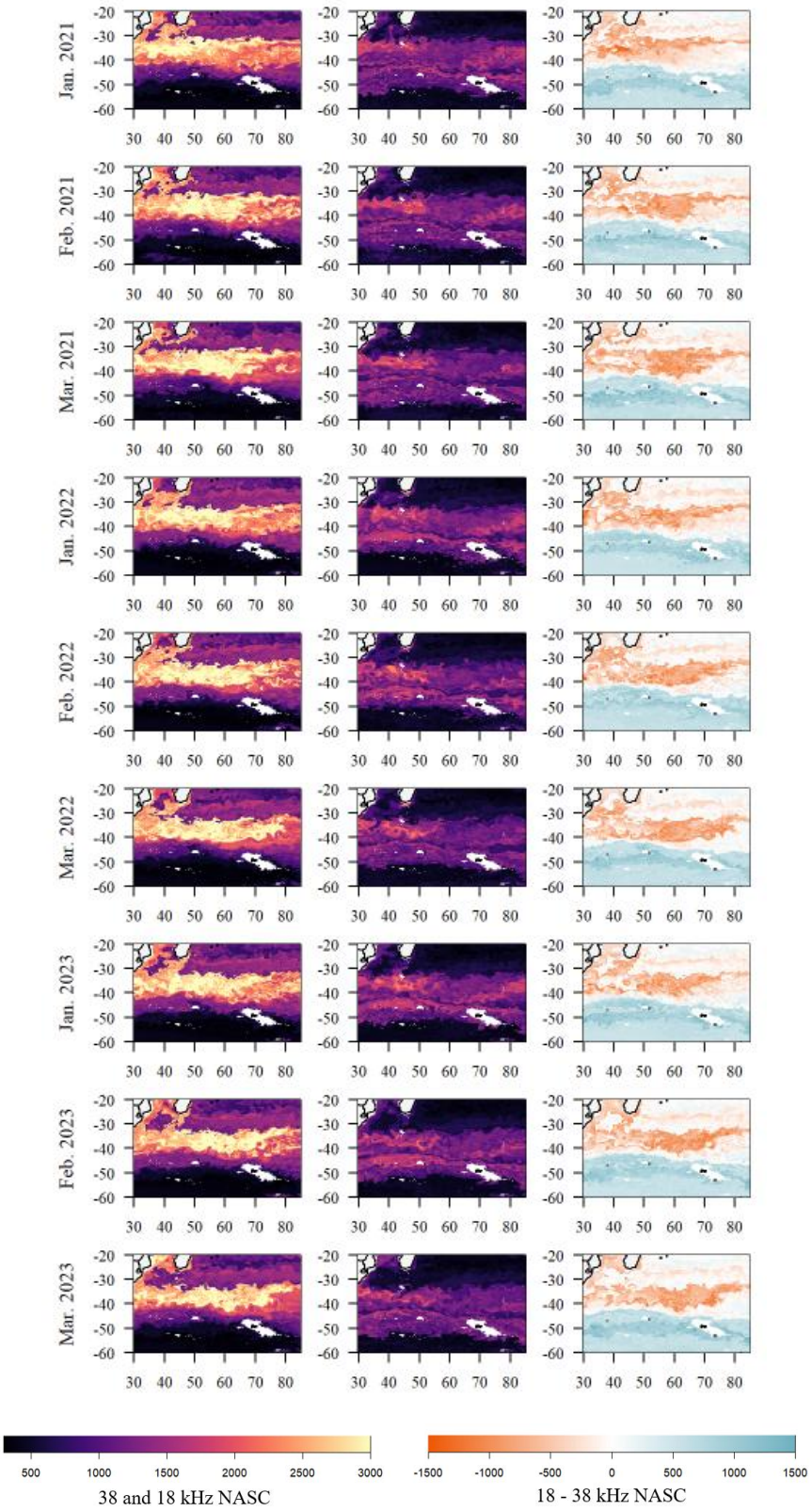

Figure S19. Integrated backscatter (NASC) at 18 kHz (left) and 38 kHz (centre), and their difference (right) for different periods between January and March and in the years 2021-2023 years. The projections were carried out following the same methodology as in the manuscript and aim to study the temporal variability of the results compared to the projection shown in the manuscript, which is the average of these predictions.

From the monthly maps, we computed mean maps for 18 and 38 kHz, as well as their differences, showing the mean NASC patterns for the austral summer of 2021, 2022 and 2023 (Figure 3, S20, S21).

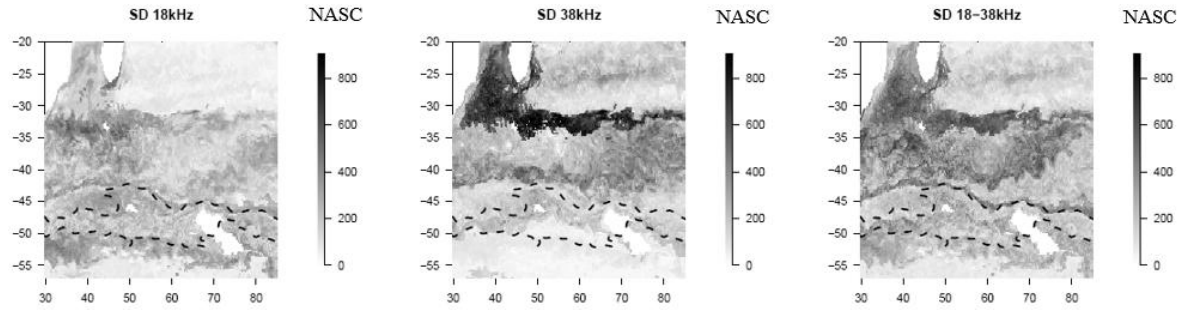

Figure S20. Standard deviation maps of integrated backscatter (NASC) at 18 kHz (left) and 38 kHz (centre), and their difference (right), for different periods between January and March in the years 2021–2023.

Daytime and nighttime patterns for 38 kHz NASC share similarities, with the highest and intermediate values observed north of the Subantarctic Front (SAF) and the lowest values found south of the SAF (Figure 3 and S21). The 18 kHz NASC suggests an enrichment of pelagic fauna acoustic biomass in temperate and subtropical zones, particularly at night.

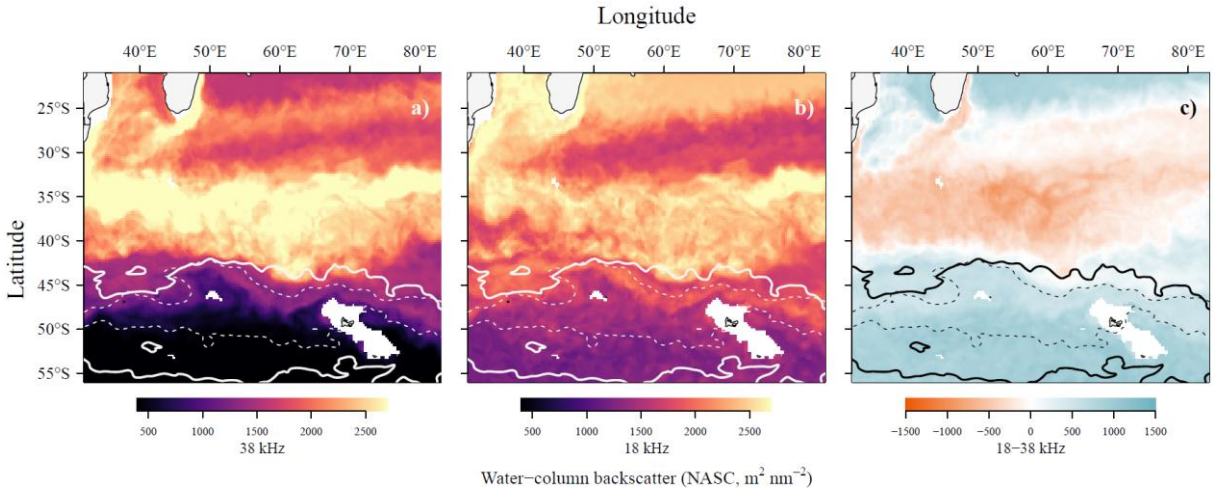

Figure S21. Averaged nighttime water-column backscatter, a proxy of animal biomass (Nautical Area Scattering Coefficient; NASC, m^2 nmi^{-2}), integrated from 25 to 1000 m depth, measured at (a) 38 kHz, (b) 18 kHz, and (c) the difference between 18 and 38 kHz. Dotted lines on the map represent the Subantarctic Front and the Polar Front (Park et al. 2019). Solid lines delineate the 75th percentile for Areas of Ecological Significance identified using marine predator trajectories (Hindell et al. 2020). In panel (c), note how pelagic fauna changes its frequency response across latitude. North (south) of the Subpolar Front is dominated by 38 kHz (18 kHz).

The observed differences in day and night distributions between north and south of the SAF reveal the influence of depth on resonance, adding further uncertainty to cross-province sonar data comparisons (Figure S22).

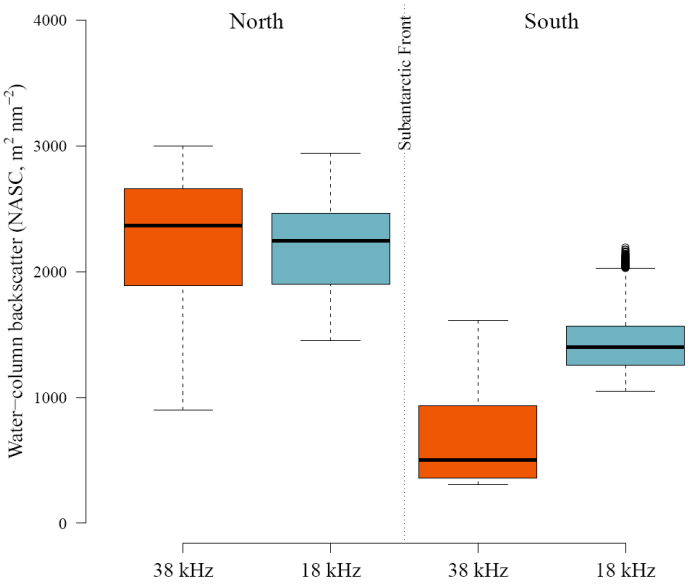

Figure S22. Nighttime water-column backscatter at 38 and 18 kHz in Nautical Area Scattering Coefficient (NASC, m^2 nmi^{-2}), integrated from 25 to 1000 m depth. Values are provided for regions north and south of the Subantarctic Front (~45°S) between 30°S and 55°S.

3. Scattering models

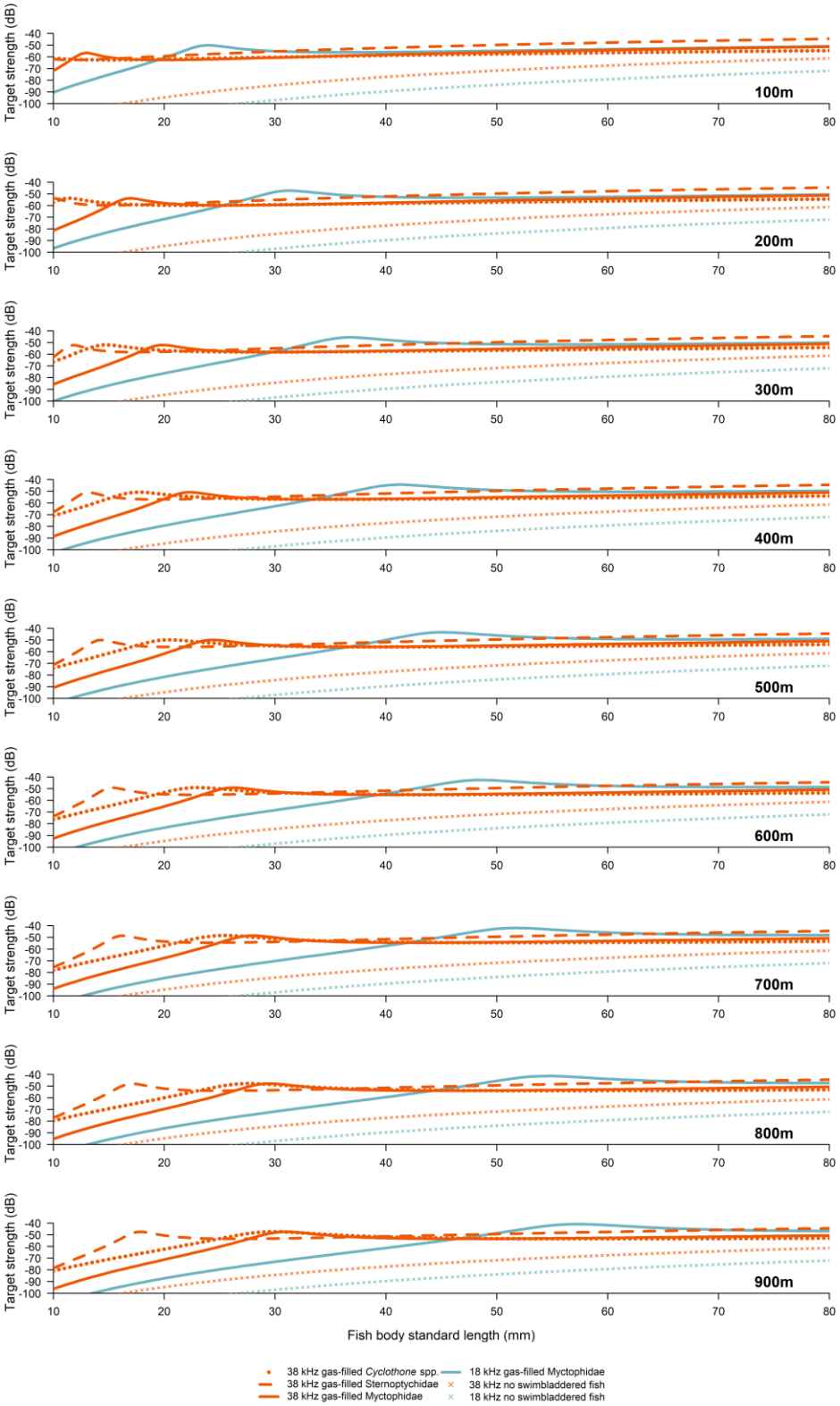

Figure S23. Modelled target strength of lanternfish (Myctophidae), hatchetfish (Sternoptychidae) and *Cyclothone* species, assuming body lengths ranging from 10 to 80 mm and a vertical distribution between 100 and 900 m. Resonance at 18 kHz was only attributed to lanternfish, as the swimbladders of hatchetfish and *Cyclothone* species are unlikely to exceed an equivalent spherical radius of 1 mm (~38 mm standard length), and are threfore unlikely to resonate at this frequency (Marshall 1960; Kleckner and Gibbs 1978).

4. Describing samples from trawl nets

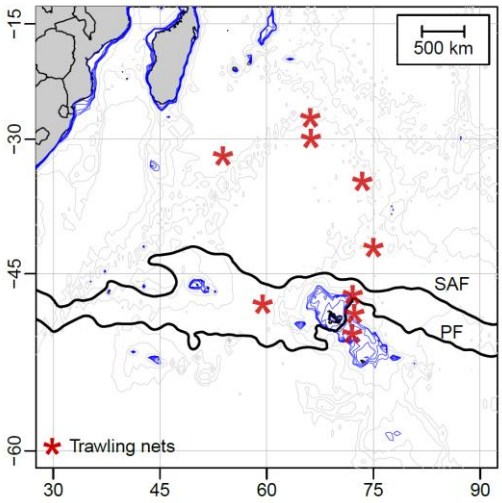

Figure S24. (Left) Locations of selected trawl stations. The Subantarctic Front (SAF) and Polar Front (PF) are shown as black lines. Blue lines represent isobaths from 200 to 1000 m, with 200 m intervals. Grey lines indicate isobaths from 1000 to 5000 m, with 1000 m intervals.

Table S3. Mesopelagos trawl stations summary.

Station	Latitude (°S)	Longitude (°E)	Date	Time (UTC)	Duration (min)	Depth targeted (m)
MESO2022_02	31.98	53.87	11/02/2022	17:09:00	79	500
MESO2022_07	47.9	59.44	16/02/2022	12:13:00	65	445
MESO2022_10	50.63	72.05	22/02/2022	03:21:00	73	450
MESO2022_11	48.8	72.35	22/02/2022	17:13:00	69	560
MESO2022_12	46.98	72.11	23/02/2022	20:02:00	72	580
MESO2022_13	42.27	75.04	25/02/2022	16:12:00	81	660
MESO2022_14	35	73.47	27/02/2022	18:55:00	76	530
MESO2022_15	29.88	66.22	01/03/2022	16:11:00	73	540
MESO2022_16	27.32	66.16	02/03/2022	09:24:00	71	530

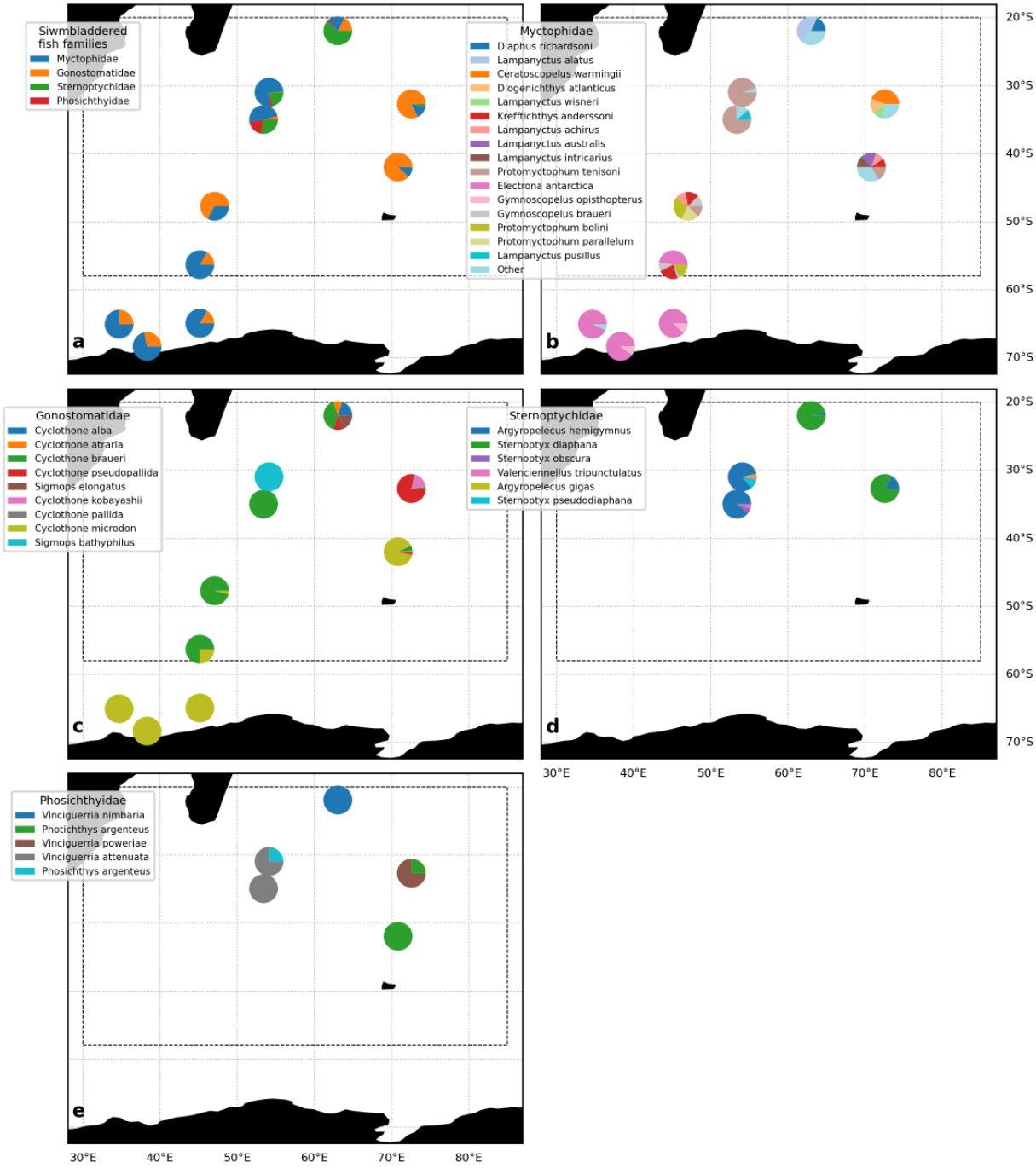

Figure S25. Relative abundance of deep pelagic fish from historical sampling in the study area. Maps show (a) the main swimbladdered fish families according to Marshall (1960), followed by the species abundance of these families: (b) Myctophidae, (c) Gonostomatidae, (d) Sternoptychidae, and (e) Phosichthyidae. Data were recovered from the Scripps Marine Vertebrate Collection and from Iwami and Kubodera (1990). All samples were collected using IKMT oblique hauls exceeding 800 m depth. For visualisation purposes, Myctophidae species with abundances below 5% are grouped together and labelled as "Other".

References

Godard, M., Manté, C., Guinet, C., Picard, B. and Nerini, D., 2020. Diving behavior of mirounga leonina: a functional data analysis approach. Frontiers in Marine Science, 7, p.595.

Iwami, T., and Kubodera, T. (1990). Mesopelagic fish collected with 10-foot IKPT in the Indian sector of the Antarctic Ocean and its neighboring waters during the JARE-28 cruise, 1987 (Eleventh Symposium on Polar Biology). In Proceedings of the NIPR Symposium on Polar Biology (Vol. 3, pp. 64-70). National Institute of Polar Research.

Kleckner, R., Gibbs, R., 1972. Swimbladder Structure of Mediterranean Midwater Fishes and a Method of Comparing Swimbladder Data with Acoustic Profiles, in: Mediterranean Biological Studies Final Report. Smithsonian Institution.

MacLennan, D.N., Fernandes, P.G. and Dalen, J., 2002. A consistent approach to definitions and symbols in fisheries acoustics. ICES Journal of Marine Science, 59(2), pp.365-369.

Marshall, N., 1960. Swimbladder structure of deep-sea fishes in relation to their systematics and biology, Discovery Reports, Vol. XXXI.

Park, Y.-H., Park, T., Kim, T.-W., Lee, S.-H., Hong, C.-S., Lee, J.-H., Rio, M.-H., Pujol, M.I., Ballarotta, M., Durand, I., Provost, C., 2019. Observations of the Antarctic Circumpolar Current over the Udintsev Fracture Zone, the narrowest choke point in the Southern Ocean. J. Geophys. Res. Oceans 124, 4511–4528. https://doi.org/ 10.1029/2019JC015024.

Pauthenet, E., Roquet, F., Madec, G., Guinet, C., Hindell, M., Mcmahon, C.R., Harcourt, R. and Nerini, D., 2018. Seasonal meandering of the Polar Front upstream of the Kerguelen Plateau. Geophysical Research Letters, 45(18), pp.9774-9781.